EMBO Journal 33.7 (2014): 762-778

DOI: 10.1002/embj.201386392

In vivo inhibition of the mitochondrial H^+-ATP synthase in neurons promotes metabolic preconditioning

Laura Formentini[1,2,3], Marta P. Pereira[1], Laura Sánchez-Cenizo[1,2,3], Fulvio Santacatterina[1,2,3], José J. Lucas[1,4], Carmen Navarro[5], Alberto Martínez-Serrano[1] and José M. Cuezva[1,2,3], *

[1]Departamento de Biología Molecular, Centro de Biología Molecular Severo Ochoa, Consejo Superior de Investigaciones Científicas-Universidad Autónoma de Madrid (CSIC-UAM); [2]Centro de Investigación Biomédica en Red de Enfermedades Raras (CIBERER), ISCIII; [3]Instituto de Investigación Hospital 12 de Octubre, Universidad Autónoma de Madrid, 28049 Madrid, Spain; [4]Centro de Investigación Biomédica en Red de Enfermedades Neurodegenerativas (CIBERNED), ISCIII; [5]Departamento de Patología y Neuropatología, Instituto de Investigación Biomédica de Vigo (IBIV), Vigo, Spain.

*, To whom correspondence should be addressed:
Prof. José M. Cuezva,
Centro de Biología Molecular Severo Ochoa, Universidad Autónoma de Madrid,
28049 Madrid, Spain.
Phone: 34-91 196 4618
Fax: 34-91 196 4420
E-mail: jmcuezva@cbm.uam.es

Running title: IF1 signals neuronal survival

Character count: 52,949 including spaces/excluding references

Abstract.

A key transducer in energy conservation and signaling cell death is the mitochondrial H^+-ATP synthase. The expression of the ATPase Inhibitory Factor 1 (IF1) is a strategy used by cancer cells to inhibit the activity of the H^+-ATP synthase to generate a ROS signal that switches on cellular programs of survival. We have generated a mouse model expressing a mutant of human IF1 in brain neurons to assess the role of the H^+-ATP synthase in cell death *in vivo*. The expression of hIF1 inhibits the activity of oxidative phosphorylation and mediates the shift of neurons to an enhanced aerobic glycolysis. Metabolic reprogramming induces brain preconditioning affording protection against quinolinic acid-induced excitotoxicity. Mechanistically, preconditioning involves the activation of the Akt/p70S6K and PARP repair pathways and Bcl-xL protection from cell death. Overall, our findings provide the first *in vivo* evidence highlighting the H^+-ATP synthase as a target to prevent neuronal cell death.

Keywords: Brain preconditioning / Energy metabolism / H+-ATP-synthase / Inhibitory Factor 1 (IF1) / Mitochondria.

Introduction.

The H^+-ATP synthase of the inner mitochondrial membrane is a master regulator of energy metabolism and cell fate. In oxidative phosphorylation (OXPHOS) the H^+-ATP synthase utilizes the H^+ electrochemical gradient generated by the respiratory chain to synthesize most of the ATP that is required to sustain cellular activities of the differentiated aerobic cell. Many findings corroborate the molecular and functional integration of OXPHOS (Dey & Moraes, 2000; Tomiyama et al., 2006), and specifically of the H^+-ATP synthase (Alavian et al., 2011; Chen et al., 2011; Matsuyama et al., 1998; Santamaria et al., 2006; Shchepina et al., 2002) with cell death. In fact, apoptosis has been shown to be strictly dependent upon subunits of the H^+-ATP synthase in yeast, mammals and plants (Chivasa et al., 2011; Gross et al., 2000; Matsuyama et al., 1998). The point of no return in cell death is the permeabilization of the inner mitochondrial membrane to low molecular weight solutes, through opening of the so-called permeability transition pore (PTP) (Di Lisa et al., ; Galluzzi et al., 2009). Although the molecular composition of the PTP remains unknown recent findings support that the high-conductance channel is composed by dimers of the H^+-ATP synthase (Giorgio et al., 2013), consistent with the finding that subunit c of the F0-channel of the H^+-ATP synthase is required for the activity of the PTP (Bonora et al., 2013). Cyclophilin D that regulates the activity of the PTP also interacts and regulates the activity of the H^+-ATP synthase (Giorgio et al., 2009).

Down-regulation of the H^+-ATP synthase is functionally linked to resistance to chemotherapy in cancer cells (Hernlund et al., 2009; Li et al., 2010; Sanchez-Arago et al., 2013a; Shin et al., 2005) consistent with the emerging role of the mitochondrial synthase in the execution of cell death. More recently, cancer cells have been shown to escape from death by inhibiting the activity of the H^+-ATP synthase by the

overexpression of the ATPase Inhibitory Factor 1 (IF1) (Faccenda et al., 2013; Formentini et al., 2012; Sanchez-Arago et al., 2013b), that mimics the inhibitory effect of oligomycin (OL) in apoptosis (Matsuyama et al., 1998; Santamaria et al., 2006; Shchepina et al., 2002). IF1 is the physiological inhibitor of the mitochondrial H^+-ATP synthase (Gledhill et al., 2007). Mechanistically, cell survival results from rewiring of energy metabolism and nuclear reprogramming due to a reactive oxygen species (ROS) signal that is produced in mitochondria after the IF1-mediated inhibition of the H^+-ATP synthase (Formentini et al., 2012; Sanchez-Arago et al., 2013b).

We present a mouse model expressing a mutant of human IF1 (hIF1) in neurons under the control of a doxycyclin-regulated promoter. The purpose of this model was to inhibit by the most effective way the activity of the H^+-ATP synthase *in vivo*. Studies in total brain, isolated mitochondria and primary neuronal cultures demonstrate that over-expression of hIF1 partially inhibits oxidative phosphorylation triggering an adaptive metabolic response that results in increased aerobic glycolysis. The IF1-mediated metabolic reprogramming results in brain preconditioning and involves a mild oxidative stress that protects neurons from excitotoxic damage, enhancing motor behavior. Overall, our findings provide the first demonstration that links the inhibition of the H^+-ATP synthase with protection from neuronal damage *in vivo*, highlighting the pivotal role that the engine of OXPHOS has as a cell death regulator.

Results.

A mouse model to inhibit the neuronal H^+-ATP synthase *in vivo*. To assess the role of OXPHOS in neurons we generated a transgenic mouse (H^+) that integrates in its genome the mutant H49K of the human ATPase Inhibitory Factor 1 (hIF1) under a tetracycline regulated promoter (TRE-H49K) (Figure 1A). The H49K mutant has a higher binding affinity for the β-catalytic subunit of the H^+-ATP synthase (Cabezon et al., 2000). Double-transgenic Tet Off mice (H^+/T^+) were generated by breeding H^+ animals with CamKII-tTA mice (T^+) that express the tTA transgene (Figure 1A) in neurons. Western blots (Figure 1A) and immunohistochemistry of coronal brain slices (Figures 1B, S1 and S2) revealed that only the H^+/T^+ genotype expresses hIF1 in mitochondria of neurons, resulting in ~3-fold increase in the total cellular content of IF1 (Figure 1A). The expression of hIF1 did not affect the expression of other mitochondrial proteins (Figures 1C and S3). However, the concentration of ATP was significantly diminished in the brain of H^+/T^+ mice when compared to controls (Figure 1D). These changes were accompanied by an increased concentration of AMP (Figure 1D) and the concurrent phosphorylation of the metabolic sensor AMPK (Figure 1E) in the brain of H^+/T^+ mice. Interestingly, a significant increase in the expression of the glycolytic enzymes GAPDH and LDH-A (Figure 1E) was observed in brain extracts of H^+/T^+ mice. Despite these differences, H^+/T^+ mice were born in the expected Mendelian ratios and were normal in appearance, home-cage behavior, reproduction and longevity up to one year follow up.

hIF1 inhibits the H^+-ATP synthase. The hydrolytic activity of the H^+-ATP synthase was significantly reduced in isolated brain mitochondria from H^+/T^+ mice when compared to controls (Figure 1F). Consistently, $TMRM^+$ staining after the administration of antimycin A revealed a minor capacity of mitochondria from H^+/T^+

mice to sustain the membrane potential (ΔΨm) (Figure 1G). Likewise, oxygen consumption rates revealed that both State 3 (ADP-stimulated), uncoupled (FCCP-induced) and OL sensitive respiration were significantly diminished when compared to controls (Figure 2A). The latter is consistent with the inhibition of the synthase activity of the ATP synthase by the expression of hIF1. No relevant differences were observed in ΔΨm in H^+/T^+ mice when compared to controls (Figures 1G and 2B). However, the addition of ADP triggered a larger ΔΨm depolarization in mitochondria of wild type *versus* H^+/T^+ mice (Figure 2B), also consistent with the partial inhibition of the synthase activity of the H^+-ATP synthase by hIF1. A mild increase in the carbonylation of specific proteins (Figure 2C) and in the basal levels of catalase, SOD1 and SOD2 (Figure 2D) was observed in the brain of H^+/T^+ mice when compared to controls. However, no significant differences in GSH and GSH/GSSG ratio were observed (Figure 2E), showing that the oxidative stress induced by hIF1 expression is of mild intensity.

hIF1 inhibits cytochrome *c* oxidase activity. No relevant differences were noted in the content of native Complexes I, II, III and V in mitochondria between H^+/T^+ mice and controls (Figure 2F). Interestingly, mitochondria of H^+/T^+ mice showed no formation of supercomplex containing Complex IV (Figure 2F). In fact, most of Complex IV migrated as monomer (Figure 2F). Consistent with the role of supercomplexes in the rate of respiration (Acin-Perez et al., 2008; Lapuente-Brun et al., 2013), the enzymatic activity of Complex IV was significantly diminished in mitochondria of H^+/T^+ mice (Figure 2G). No differences were noted in the activities of Complex I and Complex II+III between both phenotypes (Figure 2G).

hIF1 promotes metabolic reprogramming and ROS signaling in cortical neurons. Only primary cultures of cortical neurons (Figure S4) derived from H^+/T^+

embryos expressed hIF1 (Figure 3A-C). Expression of hIF1 resulted in a significant decrease in the cellular content of ATP (Figure 3D) and in the activity of the H^+-ATP synthase (Figure 3E). This effect was not observed in 4d cultures (Figure 3E), when neurons are not yet expressing hIF1 (Figure 3B). The expression of hIF1 resulted in a significant increase in aerobic glycolysis as assessed by the rate of lactate production (Figure 3F). OL induced aerobic glycolysis only in neurons derived from control animals (Figure 3F), supporting that hIF1 is stimulating aerobic glycolysis to its maximum rate (Figure 3F). Analysis of the expression of PK-M2, LDH-A and GAPDH confirmed the induction of glycolysis in H^+/T^+ neurons when compared to wild type cultures (Figure 3G). Basal fluorescence did not show significant differences between H^+/T^+ and controls (Figures 3H, S5 and S6), suggesting that there is no major difference in $\Delta\Psi m$. Consistent with the inhibition of both the synthase and hydrolase activity of the H^+-ATP synthase by hIF1, we observed that $\Delta\Psi m$ changes in response to OL were lower (Figure S5) whereas those to antimycin A were higher (Figure S6) in H^+/T^+ cultures than in control. The production of superoxide radical was enhanced in H^+/T^+ neurons when compared to wild type (Figure 3I). An increase in the carbonylation of specific neuronal proteins was observed (Figure 3J) consistent with a higher basal production of ROS in H^+/T^+ neurons and with data in brain homogenates (Figure 2C).

hIF1-mice are protected from quinolinic acid-induced brain damage. To assess the role of H^+-ATP synthase in cell death *in vivo*, one year old control and hIF1 expressing mice received an injection of quinolinic acid into the left striatal region of the brain (Martinez-Serrano & Bjorklund, 1996; Schwarcz et al., 2012). Weight loss after injury (Figure 4A), spleen volume contraction (Figure 4B), and enlargement of the ipsilateral ventricle (Figure 4C), which are respective indexes of general impairment of animal health, monocyte recruitment and tissue loss suggest that hIF1 expressing mice

are partially protected from excitotoxicity. Hematoxylin-eosin stained brain sections also revealed a significant ~50% reduction in the lesion area in H^+/T^+ mice (Figure 4D). The reduced expression of the neuronal markers DARPP-32 (Figure 4E) and NeuN (Figure S7) in the brain of controls further support a higher neuronal protection in H^+/T^+ mice. Quantification of microglia (Figure 4E, Iba-1, red staining and Figure S8) and phagocytes (Figure 4E, Ed-1, green staining and Figure S8) revealed a significant increase in gliosis in control when compared to H^+/T^+ mice suggesting that hIF1 protects neurons from damage and hence from the subsequent local inflammation.

Neurological evaluation indicates a better performance in hIF1 mice. No differences in locomotor performance were observed between control and H^+/T^+ mice before quinolinic acid administration (Figure S9A-F). However, three locomotor tests showed that H^+/T^+ mice are partially protected from quinolinic acid-induced damage and maintained lower deviation from pre-surgical values than control animals (Figure S9 and Supplementary videos for control and hIF1 expressing mice). Paw usage contralateral to the brain lesion (right) was significantly diminished in control animals when compared to H^+/T^+ mice (Figure S9A). No differences were noted in the use of the ipsilateral forelimb (left) (Figure S9B). Gate analysis revealed that control mice showed an increased stride length of the contralateral forelimb (Figure S9C) and in the coefficient of variation for base width of the hind limbs (Figure S9D) when compared to H^+/T^+ mice in the "footprint" test (Carter et al., 1999). After lesion all animals showed an increase in the number of paw-slips in the grid test (Brooks & Dunnett, 2009) but as early as 4 days post-surgery H^+/T^+ mice were able to walk through the grid with a significant lower number of paw slips (Figure S9E). The motility index of H^+/T^+ mice was unaltered by lesion (Figure S9F). However, control mice were less prone to explore than H^+/T^+ mice suggesting a severe motor impairment (Figure S9F) (Supplemental

videos for control and hIF1 expressing mice). Overall, H^+/T^+ mice showed lower deviation from pre-surgical values than control animals.

hIF1 protects from quinolinic acid-induced cell death. FluoroJade B positive neurons both in the core and penumbra region of the lesion were significantly augmented in control when compared to H^+/T^+ mice (Figure 5A). Analysis of apoptotic cell death by the determination of caspase 3 activation confirmed that hIF1 expressing neurons were protected from apoptosis in the penumbra (Figure 5B). Most of the toxic cascades stimulated by quinolinic acid implicate the formation of ROS (Schwarcz et al., 2012). Consistently, the GSH content in the damaged hemisphere was highly reduced when compared to the non-stressed tissue (compare Figure 5C versus Figure 2D). Remarkably, both the GSH content and the GSH/GSSG ratio were significantly higher in the affected hemisphere of hIF1 expressing mice than in controls (Figure 5C).

hIF1 signals the activation of neuroprotection pathways. Phosphorylation of Akt is part of the survival signaling pathway induced in cells confronted with mitochondrial respiration defects and/or mild oxidative stress (Leslie, 2006; Pelicano et al., 2006). Consistently, the phosphorylation of Akt was significantly augmented in both brain hemispheres of mice expressing hIF1 (Figure 5D). We also observed an enhanced phosphorylation of the pro-survival p70S6K in both brain hemispheres (Figure 5D) and enhanced expression of *c-fos* in the damaged area of H^+/T^+ mice (Figure 5E). Moreover, the content of IκBα, which is the negative regulator of NFκB transcription factor, was significantly diminished in the damaged hemisphere of H^+/T^+ mice (Figure 5D). Changes in Ikbα expression were paralleled by opposite changes in the expression of Bcl-xL, a downstream target of NFκB that is involved in preventing cell death (Figure 5D). In contrast, the expression of the antiapototic Bcl-2 was not affected by hIF1 expression or by quinolinic acid administration (Figure 5D). Remarkably, the ATP and

ADP content in the damaged area of the left hemisphere was much lower in H^+/T^+ mice (Figure 6A). In contrast, the AMP content was significantly increased (Figure 6A). The larger drop in ATP content of H^+/T^+ mice can be explained by the enforced hIF1-mediated inhibition of the synthase activity of the H^+-ATP synthase, but could also result from higher activation of ATP consuming reactions following activation of repair mechanisms. This is consistent with a higher basal PARP activity in the brain of H^+/T^+ mice (Figure 6B), a difference that was magnified after hemispheric damage (Figure 6B).

ROS are involved in cell death. Consistent with the role of ROS in mediating neuronal excitotoxicity (Schwarcz et al., 2012) we observed that quenching ROS after glutamate induced cell-death significantly arrested cell death in primary neuronal cultures of control mice (Figure 6C). The cell death response to glutamate was much less in neurons of hIF1 expressing mice (Figure 6C). In fact, cell death was essentially the same as that of control neurons treated with the antioxidant mito Q (Figure 6C), presumably because the hIF1-mediated activation of the pro-survival signaling pathways (Figures 5D and 6B) confers a more resistant phenotype against ROS mediated cell-death.

Bcl-xL participates in hIF1-mediated protection of neuronal death. Blue-native gels confirmed the interaction of Bcl-xL with the H^+-ATP synthase (Figure 6D) in agreement with recent findings (Alavian et al., 2011; Chen et al., 2011). However, and to our surprise, we found that Bcl-xL preferentially interacts with a native protein complex that migrates with Complex I of the respiratory chain (Figure 6D). Remarkably, silencing of Bcl-xL in neurons restored the glutamate or hypoxia-driven cell death in pre-conditioned neurons of H^+/T^+ mice (Figure 6E), further supporting the

role of the anti-apoptotic Bcl-xL in neuroprotection and eventually its cross-talk with the activity of the H^+-ATP synthase.

Discussion

Herein, we demonstrate that the expression of hIF1 partially inhibits the H^+-ATP synthase activity promoting rewiring of neuronal metabolism to an enhanced aerobic glycolysis. Inhibition of the H^+-ATP synthase activates pathways to prevent apoptotic cell death. In other words, expression of hIF1 induces a state of preconditioning that prevents neuronal death after excitotoxic damage as assessed both *in vivo* and in primary cultures. These findings provide the first *in vivo* account highlighting the relevance of rewiring energy metabolism in brain preconditioning, and stress the potential value of the H^+-ATP synthase as a target for therapeutic intervention. Moreover, the transgenic H^+ mouse developed offers a valuable tool to investigate the relevance of OXPHOS impairments in mammalian tissues *in vivo*. Until recently, IF1 was considered an inhibitor of the hydrolase activity of the ATP synthase that helps to preserve cellular ATP during hypoxia or ischemia (Faccenda et al., 2013; Gledhill et al., 2007). However, previous *in vitro* studies (Husain & Harris, 1983; Lippe et al., 1988) and more recent findings *in vivo* (Formentini et al., 2012; Sanchez-Arago et al., 2013b; Sanchez-Cenizo et al., 2010; Shen et al., 2009) have stressed the role of IF1 as an inhibitor of the synthase activity of the H^+-ATP synthase. The results in this study demonstrate the *in vivo* function of hIF1 as an inhibitor of the ATP synthase and of cell death.

Since we also observed a down-regulation of respiration and of the activity and assembly of Complex IV, it can be argued that hIF1 exerts neuroprotection by its effect on the activity of the respiratory chain rather than on the ATP synthase. However, this explanation seems unlikely because the impairment of the respiratory chain is detrimental for cell survival. In fact, very recent findings (Cogliati et al., 2013) have highlighted that the disassembly of respiratory chain supercomplexes leads to an

increase and not to a decrease in cell death, in agreement with our observation. Hence, we suggest that the effects of hIF1 on respiration result from feedback regulation of Complex IV activity/assembly by the inhibition of the ATP synthase, although the mechanism involved deserves further investigation. However, we cannot ruled out that hIF1 might be controlling the execution of cell death by regulating *cristae* remodeling (Cogliati et al., 2013; Faccenda et al., 2013) (Figure 7G). It is well established that dimers of the H^+-ATP synthase promote the high local curvature of the inner membrane at *cristae* ridges (Davies et al., 2012; Davies et al., 2011; Paumard et al., 2002). Recently, the genetic disruption of *cristae* shape morphology has been shown to favor apoptosis (Cogliati et al., 2013), providing a link between mitochondrial morphology and cell death. In this regard, it has been suggested that IF1 regulates the oligomeric state of the H^+-ATP synthase increasing the density of *cristae* and the formation of dimeric ATP synthase complexes (Bisetto et al., 2013; Campanella et al., 2008; Garcia et al., 2006; Minauro-Sanmiguel et al., 2005). Although this suggestion has been questioned (Fujikawa et al., 2012; Tomasetig et al., 2002; Wittig & Schagger, 2009), it is possible that the over-expression of hIF1 might contribute to stabilize *cristae* structure hence upgrading, at the structural level, the threshold for cell death (Figure 7G).

Energy metabolism in neurons is highly dependent on OXPHOS. Unexpectedly, H^+/T^+ mice revealed no symptoms of neurological dysfunction. It is likely that the energy deficit triggered by a limited OXPHOS promotes the activation of the metabolic stress sensor AMPK (Mihaylova & Shaw, 2011) and the subsequent activation of aerobic glycolysis to partially compensate ATP provision in these neurons. It is really intriguing to find that tissues that have a very high energy demand such as heart, liver and kidney are those that express higher levels of IF1 (Sanchez-Arago et al., 2013b;

Sanchez-Cenizo et al., 2010). Mouse (Figure 7A) and human neurons of the brain and cerebellum (Figure 7B-F and Figure S10) are not an exception showing a very high expression of IF1 when compared to astrocytes. Therefore, we suggest that the actual physiological function of IF1 in normal energy demanding tissues is to ameliorate apoptosis geared by the activity of the H^+-ATP synthase under cellular stressful conditions. This hypothesis is supported by previous findings in different cancer cells (Faccenda et al., 2013; Formentini et al., 2012; Sanchez-Arago et al., 2013b; Sanchez-Cenizo et al., 2010). Obviously, this idea further supports that in addition to the well characterized pH regulated binding of IF1 to the H^+-ATP synthase under depolarization conditions (Cabezon et al., 2000), the activity of IF1 is regulated in these tissues by additional mechanisms that could involve the interaction of IF1 with other proteins (Lopez-Mediavilla et al., 1993) (Figure 7G) and/or tissue-specific post-translational modifications (Zhao et al., 2011).

Inhibition of the synthase activity of the H^+-ATP synthase by IF1 is known to promote a mild ROS signal (Formentini et al., 2012; Sanchez-Arago et al., 2013b), which is consistent with the observed inhibition of the H^+-ATP synthase, the enhanced production of ROS in neuronal cultures and the increased carbonylation of brain and neuronal proteins in hIF1 expressing mice (Figure 7G). ROS are known activators of several of the pro-survival signaling pathways that we have shown to be activated in the brain of H^+/T^+ mice such as Akt/p70S6K (Datta et al., 1997; Harada et al., 2001) and NFκB (Karin, 2006; Ravati et al., 2001). The persistent mild oxidative stress in the brain of these animals could represent an additional mechanism involved in preconditioning (Iadecola & Anrather, 2011) by raising, at the functional level, the threshold at which a toxic insult will normally unlashed the molecular events that trigger cell death (Figure 7G). Indeed, we have observed that quenching ROS largely

inhibits glutamate induced neuronal cell death only in non-preconditioned cultures. The finding that IF1 protects cancer cells from chemotherapy induced apoptosis via ROS-mediated signaling (Formentini et al., 2012; Sanchez-Arago et al., 2013b) further supports this idea.

Importantly, our data show that hIF1 expressing neurons in the injured area are partially protected from cell death when compared to controls despite showing remarkably less ATP and ADP concentrations. Hence, we suggest that either the set-point of ATP availability for triggering cell death has not been reached (Galluzzi et al., 2012) or that the flux at which ATP is being produced by the stimulation of aerobic glycolysis is enough to preserve cellular functions. An enhanced activity of ATP-consuming reactions such as the induction of protein synthesis revealed by the activation of p70S6K and of repair pathways by the activation of PARP in hIF1 expressing neurons might also contribute to the depletion of the phosphorylated nucleotides in these animals. Taken as a whole, our findings indicate that a sustained partial inhibition of OXPHOS mediates the activation of protein synthesis, the induction of repair mechanisms and the prevention of apoptosis. Three behavioral locomotor tests confirm that hIF1 expressing mice show milder neurological impairment after injury.

Under conditions of cellular stress induced by different chemotherapeutic agents the mitochondrial H^+-ATP synthase generates a high intensity ROS signal that triggers apoptotic cell death (Johnson et al., 2005; Santamaria et al., 2006; Wondrak, 2009). Recent findings indicate that the H^+-ATP synthase forms part of the PTP (Bonora et al., 2013; Giorgio et al., 2013) stressing previous functional reports on the relevance of this complex of OXPHOS in cell death (Matsuyama et al., 1998; Santamaria et al., 2006; Shchepina et al., 2002) and the tangled circuitry of energy metabolism and apoptosis (Andersen & Kornbluth, 2013). Bcl-xL is the prevailing anti-apoptotic protein in the

brain (Alavian et al., 2011; Michels et al., 2013). We suggest that the over-expression of Bcl-xL after induced excitoxicity in the brain *in vivo* mediates the prevention of cell death, consistent with previous findings in cancer cells (Formentini et al., 2012; Sanchez-Arago et al., 2013b) and with the fact that the silencing of Bcl-xL reverted the protection afforded by IF1 over-expression. Moreover, Bcl-xL is also localized at the inner mitochondrial membrane where it interacts with the H^+-ATP synthase to enhance its activity by reducing futile ion cycling (Alavian et al., 2011; Chen et al., 2011). Herein, we have confirmed this interaction. We suggest that Bcl-xL might act as an additional regulator of the PTP, acting as the molecular bridge that links events at the inner and outer mitochondrial membranes. In fact, the silencing of Bcl-xL abrogates the pro-survival effect of the inhibition of the H^+-ATP synthase mediated by hIF1. Moreover, the finding that Bcl-xL also interacts with other complexes of the respiratory chain, presumably Complex I, broadens the biological relevance of this anti-apoptotic protein in the regulation of mitochondrial physiology and cellular metabolism.

CryoEM studies of the macromolecular organization of the inner membrane reveal no interaction between Complex I and the H^+-ATP synthase (Davies et al., 2011). However, cyclophilin D that favors PTP opening, binds to and regulates the activity of the H^+-ATP synthase (Giorgio et al., 2009) and affects modulation of PTP by rotenone (Li et al., 2012). These findings suggest that the metabolic and/or the structural preconditioning mediated by hIF1 increases the threshold of PTP opening by preventing the channel formation capacity of the H^+-ATP synthase (Giorgio et al., 2013) (Figure 7G). Overall, our data provide the first *in vivo* demonstration that the activity of the H^+-ATP synthase is necessary for the efficient execution of cell death. Hence, the H^+-ATP synthase not only functions as the power plant of the cell but also as a pivotal regulator of cell death.

Materials and methods.

Transgenic animals. The pCMV-SPORT6-H49K plasmid (Sanchez-Cenizo et al., 2010) containing the H49K mutant version of human IF1 was PCR amplified and the PCR product assembled into the pTRE2hyg vector (Clontech Laboratories Inc.) into the BamHI and Notl restriction sites. The TRE2hyg-H49K plasmid was digested with SexAI/BsrBI (New England Biolabs) and the 2.5Kb DNA fragment of interest purified with Elu-Quik kit (Shleicher & Schuell). Transgenic mice (TRE-H49K-25, H^+) were obtained by pronuclear microinjection of the construct by the Servicio de Trangenesis of the CNB/CBMSO (UAM, Madrid, Spain), using standard protocols. Integration of the construct was confirmed by PCR (forward, 5'-CACAGAGTAGAGAACAACTG-3'; reverse, 5'-GTTAGTAGCACACAGACAAA-3'). The Bl6-Tg(Camk2a-tTa)1Mmay/J mice (T^+), expressing the transactivator tTA in neurons (Mayford et al., 1996) were used. The Tet-Off double transgenic animals (H^+/T^+) were obtained by breeding H^+ and T^+ mice. Animals were maintained on the C57/Bl6 genetic background. To turn off the expression of hIF1, double transgenic mice were administered doxycycline (2mg/mL) in the drinking water during 15 days. Animal experiments were carried out after approval of the Institutional Review Board (Ethical Committee of the UAM, CEI-24-571) in compliance with animal policies and ethical guidelines of the European Community.

Brain mitochondria. Adult mice brain mitochondria were prepared after the permeabilization of synaptosomes with 100 μM digitonine. The purity of mitochondrial preparations was assessed by western blotting. Oxygen consumption rates in isolated mitochondria (200 μg protein) were determined in a Clark-type electrode. Glutamate plus malate (10 mM) were used as respiratory substrates in the presence or absence of 0.5 mM ADP, 6 μM OL, 5 μM FCCP and 1 μM antimycin A. The composition of the

respiration buffer is 75 mM manitol, 25 mM sucrose, 20 mM Tris-HCl, 5 mM phosphate, 0.3 mM EGTA, 0.5 mM EDTA, 100 mM KCl, 0.1% BSA, pH 7.4.

For the determination of the mitochondrial membrane potential, ~100 μg of mitochondria were charged with 100 nM $TMRM^+$ (Life Technologies). Changes in fluorescence were recorded using an Aminco-Bowman Series 2 Luminescence Spectrometer after addition of the following compounds (final concentration): 10 mM succinate, 1 mM ADP, 6 μM OL, 5 μM FCCP, 2 μM rotenone and 1 μM antimycin A.

Primary cultures of cortical neurons. Cerebral cortices were dissected from fetal mice at 16-17 days of gestation in Neurobasal Medium (NB) using the Papain Dissociation System kit (Worthington). Disrupted cortices were resuspended in NB supplemented with 10% HS and 2 mM glutamine. After 4–5 days in culture, non-neuronal cell division was halted by the addition of 3 mM cytosine arabinoside for 24 h. Neurons were identified evaluating their morphology and positive immunoreactivity to Neu-N antibody (Chemicon International Inc.; 1:1000) and studied at 9-11 days of culture. Lack of staining with an anti-glial fibrillary acidic protein GFAP (Dako Cytomation; 1:1000) revealed the absence of astrocytes in cell cultures.

The rates of lactate production and of oxygen consumption (XF24 Extracellular Flux Analyzer, Seahorse Bioscience) were determined (Sanchez-Cenizo et al., 2010). The final concentration and order of injected substances was 6 μM OL, 0.75 mM dinitrophenol (DNP), 1 μM rotenone and 1 μM antimycin A.

For the determination of the $\Delta\Psi_m$ and ROS levels, 100 nM $TMRM^+$ or 2.5 μM MitoSOX™ (Life Technologies) were respectively used in "redistribution mode" (Duchen et al., 2003). The fluorescence was analyzed by confocal microscopy using a Biorad Radiance 2000 Zeiss Axiovert S100TV using red (590/617 nm) excitation/emission wave lengths and quantified using ImageJ software. Fluorescence

intensity was quantified by removing background signal and measuring the mean fluorescence intensity in the pixels containing mitochondria in approximately the same number of cells and at least in 15 different fields per condition tested. 6 μM OL, 2 μM rotenone, 1 μM antimycin A and 5 μM FCCP were used.

Neuron transfection was done using Effectene Transfection Reagent (Quiagen) with control or Bcl-xL plasmid (Switchgear Genomics Inc.). For the determination of cell death, neurons were treated with 25 μM glutamate (Sigma-Aldrich) during 5 min or deprived of oxygen for 1h (1% O_2) in a Hypoxic Workstation H35 (Don Whitley Scientific). Neurons were incubated for 24h in the absence or presence of 20 nM Mito Q and after processed by confocal microscopy *in vivo* at 37ºC and 5% CO_2 using an Axioskop2-plus vertical microscope (Zeiss) coupled to a ccd color camera. Propidium iodide (2 μM) and calcein (1 μM) were utilized to determine cell death and viability, respectively. The number of cells was quantified in 20 fields per treatment using ImageJ software.

Adenine nucleotides. Adenine nucleotides were extracted from frozen brain powder with a 6% perchloric acid solution. Determination of ATP, ADP and AMP in frozen brain powder was carried out by standard enzymatic procedures. The ATP concentration in primary cultures was determined using the ATP Bioluminescence Assay Kit CLS II (Roche).

Protein electrophoresis, western blotting and protein carbonylation. Protein samples from brain and cellular extracts were fractionated on SDS–PAGE. Details of the antibodies used in western blots are provided in Supplementary Information. For the determination of protein carbonylation the Oxyblot Oxidized Protein Detection kit (Chemicon International Inc.) was used.

Blue native (BN)-PAGE. Protein extracts (250 μg) from control or H^+/T^+ mice brain mitochondria were solubilized in BN-loading buffer. 1g of n-dodecyl β-D-maltoside / g protein was added to the samples and protein complexes were fractionated in BN-gels after addition of 2.5 μl of the Coomassie dye suspension. Electrophoresis was performed in "deep blue" cathode buffer B at constant voltage of 70 V until one-third of the whole electrophoresis run. Buffer B was then exchanged with the buffer "light blue". Electrophoresis was performed for other 12 h at 70 V and then 3 h at 200V. BN-loading buffer: 50 mM NaCl, 1 mM EDTA, 5 mM 6-aminocaproic acid, 2% PMSF, 50 mM imidazole/HCl pH 7.0. BN-gels: acrylamide:bisacrylamide ratio ranging from 3% to 13% w/v; 0.5 M 6-Aminocaproic acid and 25 mM imidazole. Coomassie dye suspension (5% SBG-dye in 500 mM aminocaproic acid). Anode buffer: 25 mM imidazole, pH 7.0. "Deep blue" cathode buffer B: 50 mM tricine, 7.5 mM imidazole, 0.02% Serva Blue G (SBG), pH 7.5. "Light blue" cathode buffer B/10: the cathode buffer B with a ten times lower dye concentration (0.002% SBG).

Determination of enzyme activities. Brain mitochondria resuspended in respiration buffer containing 1% Triton X-100 were used for the spectrophotometric determination of complex I, II+III, IV and V activities as described (Barrientos et al., 2009).

Glutathion determination. The brain GSH and GSSG concentrations were determined using the Glutathione Assay Kit (BioVision Inc.).

Animal surgery and histology. One year old control (n = 10) and H^+/T^+ (n = 10) male mice were used for surgery. To induce excitotoxic damage all animals received a single 0.5 μl dose of 20 nmol of quinolinic acid by stereotaxical injection into the left striatum. Coordinates (mm) AP (anteroposterior from bregma) = +0.25, ML = 2.75, D-V (vertical from dura) = -2.5 at a speed of 1μl/minute. The right hemisphere did not

receive any surgery and served as histological control. Twenty days after the lesion mice were sacrificed, transcardially perfused with 3% paraformaldehyde and cryoprotected with 30% sucrose. Sections (30 μm thick) were taken in the coronal plane, stained with hematoxylin-eosin and processed for immunohistochemistry.

Evaluation of animal behavior. Animal behavior was evaluated by footprint, grid and cylinder tests in a blinded way before surgery and every three days post-surgery until day of sacrifice (21^{th} day). Gait abnormalities were detected by analysis of motor coordination and synchrony using the "footprint" test (Carter et al., 1999). Briefly fore and hind paws were dipped into water soluble ink of different colors and animals were left free to walk over absorbent paper in a straight line. Analysis included measurement of stride length, width of the base of support for the hind limbs and paw angle (fore and hind). Gait variability was studied using the coefficient of variation (CV) calculated from the equation 100 × standard deviation/mean value. For the grid test: Mice were left free to walk across a horizontal grid (size: 20x30cm, 10mm wire mesh). The number of ipsilateral and contralateral paw slips through the grid were counted and the motility index was calculated from the equation: percentage of the time spent moving/(number of foot faults + number of stops) (Brooks & Dunnett, 2009). For the cylinder test: mice were placed in a perspex cylinder (9 cm diameter, 15cm tall) for 5 minutes and recorded with a videocamera. Paw usage was studied by measuring the number of forelimb wall contacts made with each paw when rearing (Brooks & Dunnett, 2009). Data is presented as number of contacts per minute for left, right and both forepaws simultaneously.

Immunofluorescence/confocal microscopy and immunohistochemistry. Free-floating brain slices were incubated with blocking buffer (3% BSA and 0.1% Triton X-

100 in PBS) for 1 h at RT and then incubated overnight at 4°C with the primary antibodies specified.

The primary antibodies used were: anti-NeuN (1:100) and Fluoro Jade B (0.001%) from Millipore Bioscience Research Reagents; anti-GFAP (1:1000) from Dako Cytomation; anti-Iba-1 (1:500) from Wako; anti-Ed-1 (1:100) and anti-c-fos (1:100) from Santa Cruz Biotechnology, Inc.; anti-DARP-32 (1:500) from Chemicon International Inc. and anti-caspase-3 (1:100) from Cell Signaling Technology Inc. Secondary Cy-3/Cy-5/Cy-2-conjugated antibodies were used (Millipore Bioscience Research Reagents). Cellular fluorescence was analyzed by confocal microscopy using a Biorad Radiance 2000 Zeiss Axiovert S100TV using green (498/516 nm), red (590/617 nm) or blue (642/661 nm) excitation/emission wave lengths. The area and intensity of fluorescence were quantified by ImageJ software.

Mice brain slices were incubated in 3% H_2O_2 in methanol for 10 min at room temperature to block the endogenous peroxidase activity. Antigens were retrieved by incubation in Dako Retrieval Solution (Dako Cytomation) for 2 min at 98ºC. The anti-IF1 (1:200) and anti-β-F1-ATPase (1:20,000) were used for immunohistochemistry using the peroxidase based EnVisionTM FLEX Mini kit High pH (Dako Cytomation). Specimens were then incubated with diaminobenzidine chromogenic substrate (Dako Cytomation) for 5 min at room temperature. To assess the expression of IF1 in human brain, 3 μm paraffin sections obtained from post mortem CNS specimens from a patient with no neurologic disease were processed for immunocytochemistry. Sections were automatically deparaffinised and immunostained with an Autostainer Link instrument from Dako (Carpinteria). Antigenic retrieval was performed at low pH, incubated with anti-IF1 at 1/100 dilution during 30 minutes and visualized with EnVision Flex system

from Dako (Carpinteria). Sections were observed with a Leica DMRE light microscope.

Statistical Analysis. Statistical analyses were performed using a two-tailed Student's t-test. ANOVA with post hoc Dunnett's test were used for multiple comparisons to the control, using the SPSS 17.0 software package. The results shown are means ± SEM. A $p < 0.05$ was considered statistically significant.

Acknowledgments

The authors acknowledge the technical support provided by M. Chamorro, C. Nuñez de Arenas, E. Casas, C. Cuevas and Z. Ortega. LF is supported by "Fundación de la Asociación Española Contra el Cáncer" (AECC). This work was supported by grants from the MEC (BFU2010-18903), CIBERER and by Comunidad de Madrid (S2011/BMD-2402) to JMC; MINECO (PLE2009-0101 and SAF2010-17167), TerCel (RD12/0019/0013) and Neurostem-CM (S2010-BMD-2336) to AMS and ISCIII grant PI 10/02628 to CN, Spain. The CBMSO receives an institutional grant from Fundación Ramón Areces.

Author contributions

LF and JMC designed research; LF, MPP, LSC, FS, JJL and CN performed research; LF, MPP, CN, AMS and JMC analyzed data; LF and JMC wrote the paper.

Conflict of Interest

The authors declare no conflict of interests.

References

Acin-Perez R, Fernandez-Silva P, Peleato ML, Perez-Martos A, Enriquez JA (2008) Respiratory active mitochondrial supercomplexes. *Mol Cell* **32**: 529-539

Alavian KN, Li H, Collis L, Bonanni L, Zeng L, Sacchetti S, Lazrove E, Nabili P, Flaherty B, Graham M, et al. (2011) Bcl-x(L) regulates metabolic efficiency of neurons through interaction with the mitochondrial F(1)F(O) ATP synthase. *Nat Cell Biol* **13**: 1224-1233

Andersen JL, Kornbluth S (2013) The tangled circuitry of metabolism and apoptosis. *Mol Cell* **49**: 399-410

Barrientos A, Fontanesi F, Diaz F (2009) Evaluation of the mitochondrial respiratory chain and oxidative phosphorylation system using polarography and spectrophotometric enzyme assays. *Curr Protoc Hum Genet* **19**: Unit19 13

Bisetto E, Comelli M, Salzano AM, Picotti P, Scaloni A, Lippe G, Mavelli I (2013) Proteomic analysis of F1F0-ATP synthase super-assembly in mitochondria of cardiomyoblasts undergoing differentiation to the cardiac lineage. *Biochim Biophys Acta* **1827**: 807-816

Bonora M, Bononi A, De Marchi E, Giorgi C, Lebiedzinska M, Marchi S, Patergnani S, Rimessi A, Suski JM, Wojtala A, et al. (2013) Role of the c subunit of the FO ATP synthase in mitochondrial permeability transition. *Cell Cycle* **12**: 674-683

Brooks SP, Dunnett SB (2009) Tests to assess motor phenotype in mice: a user's guide. *Nat Rev Neurosci* **10**: 519-529

Cabezon E, Butler PJ, Runswick MJ, Walker JE (2000) Modulation of the oligomerization state of the bovine F1-ATPase inhibitor protein, IF1, by pH. *J Biol Chem* **275**: 25460-25464

Campanella M, Casswell E, Chong S, Farah Z, Wieckowski MR, Abramov AY, Tinker A, Duchen MR (2008) Regulation of mitochondrial structure and function by the F1Fo-ATPase inhibitor protein, IF1. *Cell Metab* **8**: 13-25

Carter RJ, Lione LA, Humby T, Mangiarini L, Mahal A, Bates GP, Dunnett SB, Morton AJ (1999) Characterization of progressive motor deficits in mice transgenic for the human Huntington's disease mutation. *J Neurosci* **19**: 3248-3257

Cogliati S, Frezza C, Soriano ME, Varanita T, Quintana-Cabrera R, Corrado M, Cipolat S, Costa V, Casarin A, Gomes LC, et al. (2013) Mitochondrial cristae shape determines respiratory chain supercomplexes assembly and respiratory efficiency. *Cell* **155**: 160-171

Chen YB, Aon MA, Hsu YT, Soane L, Teng X, McCaffery JM, Cheng WC, Qi B, Li H, Alavian KN, et al. (2011) Bcl-xL regulates mitochondrial energetics by stabilizing the inner membrane potential. *J Cell Biol* **195**: 263-276

Chivasa S, Tome DF, Hamilton JM, Slabas AR (2011) Proteomic analysis of extracellular ATP-regulated proteins identifies ATP synthase beta-subunit as a novel plant cell death regulator. *Mol Cell Proteomics* **10**: M110 003905

Datta SR, Dudek H, Tao X, Masters S, Fu H, Gotoh Y, Greenberg ME (1997) Akt phosphorylation of BAD couples survival signals to the cell-intrinsic death machinery. *Cell* **91**: 231-241

Davies KM, Anselmi C, Wittig I, Faraldo-Gomez JD, Kuhlbrandt W (2012) Structure of the yeast F1Fo-ATP synthase dimer and its role in shaping the mitochondrial cristae. *Proc Natl Acad Sci U S A* **109**: 13602-13607

Davies KM, Strauss M, Daum B, Kief JH, Osiewacz HD, Rycovska A, Zickermann V, Kuhlbrandt W (2011) Macromolecular organization of ATP synthase and complex I in whole mitochondria. *Proc Natl Acad Sci U S A* **108**: 14121-14126

Dey R, Moraes CT (2000) Lack of oxidative phosphorylation and low mitochondrial membrane potential decrease susceptibility to apoptosis and do not modulate the protective effect of Bcl-x(L) in osteosarcoma cells. *J Biol Chem* **275**: 7087-7094

Di Lisa F, Carpi A, Giorgio V, Bernardi P (2011) The mitochondrial permeability transition pore and cyclophilin D in cardioprotection. *Biochim Biophys Acta* **1813**: 1316-1322

Duchen MR, Surin A, Jacobson J (2003) Imaging mitochondrial function in intact cells. *Methods Enzymol* **361**: 353-389

Faccenda D, Tan CH, Seraphim A, Duchen MR, Campanella M (2013) IF1 limits the apoptotic-signalling cascade by preventing mitochondrial remodelling. *Cell Death Differ* **20**: 686-697

Formentini L, Sánchez-Aragó M, Sánchez-Cenizo L, Cuezva JM (2012) The mitochondrial ATPase Inhibitory Factor 1 (IF1) triggers a ROS-mediated retrograde pro-survival and proliferative response. *Mol. Cell* **45**: 731-742

Fujikawa M, Imamura H, Nakamura J, Yoshida M (2012) Assessing the actual contribution of IF1, an inhibitor of mitochondrial FoF1, to ATP homeostasis, cell growth, mitochondrial morphology and cell viability. *J Biol Chem* **287**: 18781-18787

Galluzzi L, Blomgren K, Kroemer G (2009) Mitochondrial membrane permeabilization in neuronal injury. *Nat Rev Neurosci* **10**: 481-494

Galluzzi L, Kepp O, Kroemer G (2012) Mitochondria: master regulators of danger signalling. *Nat Rev Mol Cell Biol* **13**: 780-788

Garcia JJ, Morales-Rios E, Cortes-Hernandez P, Rodriguez-Zavala JS (2006) The inhibitor protein (IF1) promotes dimerization of the mitochondrial F1F0-ATP synthase. *Biochemistry* **45**: 12695-12703

Giorgio V, Bisetto E, Soriano ME, Dabbeni-Sala F, Basso E, Petronilli V, Forte MA, Bernardi P, Lippe G (2009) Cyclophilin D modulates mitochondrial F0F1-ATP synthase by interacting with the lateral stalk of the complex. *J Biol Chem* **284**: 33982-33988

Giorgio V, von Stockum S, Antoniel M, Fabbro A, Fogolari F, Forte M, Glick GD, Petronilli V, Zoratti M, Szabo I, et al. (2013) Dimers of mitochondrial ATP synthase form the permeability transition pore. *Proc Natl Acad Sci U S A* **110**: 5887-5892

Gledhill JR, Montgomery MG, Leslie AG, Walker JE (2007) How the regulatory protein, IF(1), inhibits F(1)-ATPase from bovine mitochondria. *Proc Natl Acad Sci U S A* **104**: 15671-15676

Gross A, Pilcher K, Blachly-Dyson E, Basso E, Jockel J, Bassik MC, Korsmeyer SJ, Forte M (2000) Biochemical and genetic analysis of the mitochondrial response of yeast to BAX and BCL-X(L). *Mol Cell Biol* **20**: 3125-3136

Harada H, Andersen JS, Mann M, Terada N, Korsmeyer SJ (2001) p70S6 kinase signals cell survival as well as growth, inactivating the pro-apoptotic molecule BAD. *Proc Natl Acad Sci U S A* **98**: 9666-9670

Hernlund E, Hjerpe E, Avall-Lundqvist E, Shoshan M (2009) Ovarian carcinoma cells with low levels of beta-F1-ATPase are sensitive to combined platinum and 2-deoxy-D-glucose treatment. *Mol Cancer Ther* **8**: 1916-1923

Husain I, Harris DA (1983) ATP synthesis and hydrolysis in submitochondrial particles subjected to an acid-base transition. Effects of the ATPase inhibitor protein. *FEBS Lett* **160**: 110-114

Iadecola C, Anrather J (2011) Stroke research at a crossroad: asking the brain for directions. *Nat Neurosci* **14**: 1363-1368

Johnson KM, Chen X, Boitano A, Swenson L, Opipari AW, Jr., Glick GD (2005) Identification and validation of the mitochondrial F1F0-ATPase as the molecular target of the immunomodulatory benzodiazepine Bz-423. *Chem Biol* **12**: 485-496

Karin M (2006) Nuclear factor-kappaB in cancer development and progression. *Nature* **441**: 431-436

Lapuente-Brun E, Moreno-Loshuertos R, Acin-Perez R, Latorre-Pellicer A, Colas C, Balsa E, Perales-Clemente E, Quiros PM, Calvo E, Rodriguez-Hernandez MA, et al. (2013) Supercomplex assembly determines electron flux in the mitochondrial electron transport chain. *Science* **340**: 1567-1570

Leslie NR (2006) The redox regulation of PI 3-kinase-dependent signaling. *Antioxid Redox Signal* **8**: 1765-1774

Li B, Chauvin C, De Paulis D, De Oliveira F, Gharib A, Vial G, Lablanche S, Leverve X, Bernardi P, Ovize M, et al. (2012) Inhibition of complex I regulates the

mitochondrial permeability transition through a phosphate-sensitive inhibitory site masked by cyclophilin D. *Biochim Biophys Acta* **1817**: 1628-1634

Li RJ, Zhang GS, Chen YH, Zhu JF, Lu QJ, Gong FJ, Kuang WY (2010) Down-regulation of mitochondrial ATPase by hypermethylation mechanism in chronic myeloid leukemia is associated with multidrug resistance. *Ann Oncol* **7**: 1506-1514

Lippe G, Sorgato MC, Harris DA (1988) Kinetics of the release of the mitochondrial inhibitor protein. Correlation with synthesis and hydrolysis of ATP. *Biochim Biophys Acta* **933**: 1-11

Lopez-Mediavilla C, Vigny H, Godinot C (1993) Docking the mitochondrial inhibitor protein IF1 to a membrane receptor different from the F1-ATPase beta subunit. *Eur J Biochem* **215**: 487-496

Martinez-Serrano A, Bjorklund A (1996) Protection of the neostriatum against excitotoxic damage by neurotrophin-producing, genetically modified neural stem cells. *J Neurosci* **16**: 4604-4616

Matsuyama S, Xu Q, Velours J, Reed JC (1998) The Mitochondrial F0F1-ATPase proton pump is required for function of the proapoptotic protein Bax in yeast and mammalian cells. *Mol Cell* **1**: 327-336

Mayford M, Bach ME, Huang YY, Wang L, Hawkins RD, Kandel ER (1996) Control of memory formation through regulated expression of a CaMKII transgene. *Science* **274**: 1678-1683

Michels J, Kepp O, Senovilla L, Lissa D, Castedo M, Kroemer G, Galluzzi L (2013) Functions of BCL-X L at the Interface between Cell Death and Metabolism. *Int J Cell Biol* **2013**: 705294

Mihaylova MM, Shaw RJ (2011) The AMPK signalling pathway coordinates cell growth, autophagy and metabolism. *Nat Cell Biol* **13**: 1016-1023

Minauro-Sanmiguel F, Wilkens S, Garcia JJ (2005) Structure of dimeric mitochondrial ATP synthase: novel F0 bridging features and the structural basis of mitochondrial cristae biogenesis. *Proc Natl Acad Sci U S A* **102**: 12356-12358

Paumard P, Vaillier J, Coulary B, Schaeffer J, Soubannier V, Mueller DM, Brethes D, di Rago JP, Velours J (2002) The ATP synthase is involved in generating mitochondrial cristae morphology. *EMBO J* **21**: 221-230

Pelicano H, Xu RH, Du M, Feng L, Sasaki R, Carew JS, Hu Y, Ramdas L, Hu L, Keating MJ, et al. (2006) Mitochondrial respiration defects in cancer cells cause activation of Akt survival pathway through a redox-mediated mechanism. *J Cell Biol* **175**: 913-923

Ravati A, Ahlemeyer B, Becker A, Klumpp S, Krieglstein J (2001) Preconditioning-induced neuroprotection is mediated by reactive oxygen species and activation of the transcription factor nuclear factor-kappaB. *J Neurochem* **78**: 909-919

Sanchez-Arago M, Formentini L, Cuezva JM (2013a) Mitochondria-Mediated Energy Adaption in Cancer: The H(+)-ATP Synthase-Geared Switch of Metabolism in Human Tumors. *Antioxid Redox Signal* **19**: 285-298

Sanchez-Arago M, Formentini L, Martinez-Reyes I, Garcia-Bermudez J, Santacatterina F, Sanchez-Cenizo L, Willers IM, Aldea M, Najera L, Juarranz A, et al. (2013b) Expression, regulation and clinical relevance of the ATPase inhibitory factor 1 in human cancers. *Oncogenesis* **2**: e46

Sanchez-Cenizo L, Formentini L, Aldea M, Ortega AD, Garcia-Huerta P, Sanchez-Arago M, Cuezva JM (2010) Up-regulation of the ATPase inhibitory factor 1 (IF1) of the mitochondrial H+-ATP synthase in human tumors mediates the metabolic shift of cancer cells to a Warburg phenotype. *J Biol Chem* **285**: 25308-25313

Santamaria G, Martinez-Diez M, Fabregat I, Cuezva JM (2006) Efficient execution of cell death in non-glycolytic cells requires the generation of ROS controlled by the activity of mitochondrial H+-ATP synthase. *Carcinogenesis* **27**: 925-935

Schwarcz R, Bruno JP, Muchowski PJ, Wu HQ (2012) Kynurenines in the mammalian brain: when physiology meets pathology. *Nat Rev Neurosci* **13**: 465-477

Shchepina LA, Pletjushkina OY, Avetisyan AV, Bakeeva LE, Fetisova EK, Izyumov DS, Saprunova VB, Vyssokikh MY, Chernyak BV, Skulachev VP (2002) Oligomycin, inhibitor of the F0 part of H+-ATP-synthase, suppresses the TNF-induced apoptosis. *Oncogene* **21**: 8149-8157

Shen L, Zhi L, Hu W, Wu MX (2009) IEX-1 targets mitochondrial F1Fo-ATPase inhibitor for degradation. *Cell Death Differ* **16**: 603-612

Shin YK, Yoo BC, Chang HJ, Jeon E, Hong SH, Jung MS, Lim SJ, Park JG (2005) Down-regulation of mitochondrial F1F0-ATP synthase in human colon cancer cells with induced 5-fluorouracil resistance. *Cancer Res* **65**: 3162-3170

Tomasetig L, Di Pancrazio F, Harris DA, Mavelli I, Lippe G (2002) Dimerization of F0F1ATP synthase from bovine heart is independent from the binding of the inhibitor protein IF1. *Biochim Biophys Acta* **1556**: 133-141

Tomiyama A, Serizawa S, Tachibana K, Sakurada K, Samejima H, Kuchino Y, Kitanaka C (2006) Critical role for mitochondrial oxidative phosphorylation in the activation of tumor suppressors Bax and Bak. *J Natl Cancer Inst* **98**: 1462-1473

Wittig I, Schagger H (2009) Supramolecular organization of ATP synthase and respiratory chain in mitochondrial membranes. *Biochim Biophys Acta* **1787**: 672-680
Wondrak GT (2009) Redox-directed cancer therapeutics: molecular mechanisms and opportunities. *Antioxid Redox Signal* **11**: 3013-3069

Zhao X, Leon IR, Bak S, Mogensen M, Wrzesinski K, Hojlund K, Jensen ON (2011) Phosphoproteome analysis of functional mitochondria isolated from resting human muscle reveals extensive phosphorylation of inner membrane protein complexes and enzymes. *Mol Cell Proteomics* **10**: M110.000299

Figure legends.

Figure 1. Mice expressing hIF1 in neurons. (**A**) PCR analysis for the H49K variant of hIF1 and tTA constructs in wild type (wt), tTA (T^+), H49K (H^+) or double transgenic (H^+/T^+) mice is shown. Western blots reveal the expression of hIF1 and IF1 (12 kDa) in total brain extracts. hIF1 is only expressed in H^+/T^+ mice. β-actin expression is shown as loading control. (**B**) Immunohistochemistry (mitochondrial staining) for hIF1 and β-F1 ATPase (β-F1) in brain cortex of control (wt) and H^+/T^+ mice. Magnification 63x. (**C**) Representative blots of the expression of hIF1, heat-shock protein 60 (HSP60), and mitochondrial complexes I (NADH9), II (SDH), III (Core II), IV (COXI and COX IV) and V (β-F1) in total brain extracts of wt and H^+/T^+ mice. Two different samples per condition tested are shown. (**D**) Content of adenine nucleotides in brain extracts of control (wt, closed bars) and H^+/T^+ mice (open bars). (**E**) Western blots show the hIF1 dependent phosphorylation of AMPK (p-AMPK) and the concurrent increase in glycolytic proteins lactate dehydrogenase A (LDH-A) and glyceraldehyde-3-phosphate dehydrogenase (GAPDH) in brain extracts (see histograms to the right). Two different samples per condition tested are shown. β-F1 and HSP60 expressions are shown as loading controls. (**F**) Hydrolytic activity of the H^+-ATP synthase in isolated mitochondria from brain of control (wt, black trace) and H^+/T^+ (gray trace) mice. Where indicated, 10μM oligomycin (OL) was added. (**G**) Variation in the membrane potential ($TMRM^+$ staining) of isolated mitochondria from control (black trace) and H^+/T^+ animals (gray trace) charged with 100 nM $TMRM^+$. The effect of 1 μM antimycin A in the presence of 10 mM ATP is shown. (**D,E,F**) Bars are the mean±S.E.M. of six different samples. *, $P<0.05$ when compared to control by Student's t test. See also Figures S1, S2 and S3.

Figure 2. hIF1 impairs oxidative phosphorylation. (**A**) Polarographic profiles of isolated mitochondria from control (lower trace) and H^+/T^+ animals (upper trace). The effect of 10mM glutamate/malate, 0.5 mM ADP, 5 μM oligomycin (OL), 5 μM FCCP and 1 μM antimycin A (Ant) is shown. Histograms reveal a reduction in State III (StIII) and uncoupled (FCCP) respiration in mitochondria of H^+/T^+ mice (open bars) when compared to controls (wt, closed bars). OL-sensitive ATP synthase activity is also shown as a percentage of maximal respiration. (**B**) Variation in the membrane potential ($TMRM^+$ staining) of isolated mitochondria from control (black trace) and H^+/T^+ animals (gray trace) charged with 100 nM $TMRM^+$. The effect of 5 mM succinate, 1 mM ADP, 5 μM OL and 5 μM FCCP 1 is shown. Histograms show a larger reduction in $\Delta\Psi m$ after ADP administration in controls (wt, closed bars) when compared to hIF1 expressing mice (H^+/T^+, open bars). (**C**) Representative blot of the extent of carbonylation of total brain proteins. Two different samples per condition tested are shown. Tubulin was used as loading control. The migration of molecular mass markers is indicated to the right. Arrows (to the left) identify the migration of the two proteins used in the quantification of protein carbonylation (histograms). (**D**) Representative blots of catalase (cat), superoxide dismutase 1 and 2 (SOD1 and SOD2) expression in control (wt, closed bars) and hIF1 expressing (H^+/T^+, open bars) mice. (**E**) Cellular glutathione (GSH) and GSH/GSSG ratio in total brain. (**F**) Blue-native immunoblot analysis of mitochondrial membrane proteins visualized with antibodies against mitochondrial complexes I (NADH9), II (SDH), III (Core II), IV (COX IV) and V (β-F1-ATPase). The migration of monomers (Mon), dimers (Dim), supercomplex (SC), F1-ATPase (F1), H^+-ATP synthase (F0F1) and molecular mass markers is indicated. (**G**) Enzymatic activity of mitochondrial complex I, II+III and IV in isolated brain mitochondria of control (wt, closed bars) and H^+/T^+ (open bars) mice. (**A-G**) Bars are

the mean ± SEM of three (**A, B, D**), four (**C**) or six (**E, F**) determinations. *, P<0.05 when compared to controls by Student's t test.

Figure 3. hIF1 induced metabolic reprogramming and ROS signaling in cortical neurons. (**A**) *In vivo* phase contrast images of 9 d cultures of cortical neurons obtained from control and H^+/T^+ embryos. Magnification 40x. Representative western blot (**B**) and immunocytochemistry (**C**) show the expression of hIF1 only in 9 d neurons of H^+/T^+ mice. β-F1-ATPase (β-F1) is used as loading control. DAPI (4',6-diamidino-2-phenylindole) staining is also shown. Magnification 40x. (**D**) The cellular ATP content was determined in control (wt, closed bar) and H^+/T^+ (open bar) neuronal cultures. (**E**) Shows the oligomycin sensitive respiration (OSR) and maximal respiration in 4d and 9d neuronal cultures from control (wt, closed bar) and H^+/T^+ (open bar) embryos. (**F**) Rates of aerobic glycolysis in the absence or presence of 5 μM oligomycin (OL). (**G**) Representative blots of the expression of pyruvate kinase M2 (PKM2), lactate dehydrogenase A (LDH-A), glyceraldehyde-3-phosphate dehydrogenase (GAPDH) and heat-shock protein 60 (HSP60) in control (wt, closed bars) and hIF1 expressing (H^+/T^+, open bars) neurons (**H,I**) *In vivo* staining of $TMRM^+$ (**H,** $\Delta\Psi m$) or MitoSOX (**I,** ROS) charged mitochondria from 10d primary cultures of cortical neurons. Magnification 40x. (**J**) Representative experiment of carbonylation of proteins in primary neuronal cultures derived from control (wt) and H^+/T^+ mice. Tubulin is shown as loading control. The migration of molecular mass markers is indicated to the right. Histograms show the quantification of p35 and p29 proteins. (**D-J**) The data shown are mean ± SEM of three (**D-F, H-I**) or four (**G, J**) cultures per condition. *, P<0.05 when compared to control by Student's t test. See also Figures S4, S5 and S6.

Figure 4. hIF1 protects from quinolinic acid-induced brain damage. Animal weight loss (**A**) and spleen weight (**B**) in control (wt, closed squares) and H^+/T^+ (open squares) mice at the indicated time after surgery (**A**) or at time of sacrifice (21 day) (**B-E**). (**C**) Representative ventricular symmetry in sections of the brain from control (wt, closed bar) and H^+/T^+ (open bar) mice. Magnification 2.5x. The percentage increase in ventricle area is shown. (**D**) Brain sections stained with hematoxylin-eosin. Four different animals per condition tested are presented. The area of the lesion is indicated. Magnification 20x. Histograms show a reduction in the lesion area in H^+/T^+ mice (open bar) when compared to control (wt, closed bar) mice. Bars are the mean ± SEM. of five animals. D, dorsal; M, medial. (**E**) Representative staining of nuclei (DAPI, blue), protein phosphatase 1 (DARPP-32, white),microglia (Iba-1, red), macrophage/monocyte (Ed-1, green) antibodies the left hemisphere. Magnification 5x. Histograms show the quantification of fluorescence in controls (wt, closed bar) and H^+/T^+ (open bar) mice. (**A-E**) Bars are the mean ± SEM. of five (**C-E**) or ten (**A-B**) animals. Where indicated, numbers correspond to the identification code of the mouse. *, $P<0.05$ when compared to control by Student's t test. See also Figures S7, S8, S9 and Supplementary Videos.

Figure 5. The inhibition of the H^+-ATP synthase protects neurons from apoptosis. (**A**) Fluorojade B staining in degenerating neurons in the core and penumbra of the striatal lesion. Three different images of animals identified by numbers are presented. Magnification 20x. Histograms show a reduction of the fluorojade B positive area in H^+/T^+ (open bar) when compared to control (wt, closed bar) mice. (**B**) Activated caspase 3 staining in the penumbra of the striatal lesion in control (wt, closed bars) and hIF1 (H^+/T^+, open bars) expressing mice. Magnification 20x. Histograms show a reduction in the apoptotic area in H^+/T^+ mice. (**C**) Brain glutathione (GSH) content and GSH/GSSG

ratio in the injured area of control (wt, closed bar) and H^+/T^+ (open bar) mice. (**D**) Representative blots of the expression of protein kinase B (p-AKT, AKT), phospho p70 S6 kinase (p-P70S6), IkappaB alpha (IκBα), B-cell lymphoma-extra large (Bcl-xL) and B-cell lymphoma 2 (Bcl-2) in the right (R) and left (L) hemispheres of wt and H^+/T^+ mice. One control and two different H^+/T^+ animals are shown. (**E**) DAPI (blue), c-Fos (green) and glial fibrillary acidic protein (GFAP, red) staining of brain slices of the left hemisphere after three weeks post-surgery. Magnification 5x. Histograms show the quantification of fluorescence in control (wt, closed bar) and H^+/T^+ (open bar) mice. D, dorsal; M, medial. (**A-E**) Determinations were carried out at 21 day post-surgery. Bars are the mean ± SEM. of three (**E**), four (**D**) or five (**A-C**) animals. * and #, $P<0.05$ when compared to the right or left hemisphere of controls, respectively.

Figure 6. Bcl-xL is involved in hIF1-mediated protection of neurons. (**A**) Content of adenine nucleotides in the injured area of the left hemisphere of control (wt, closed bars) and hIF1 expressing (H^+/T^+, open bars) mice. *, $P<0.05$ when compared to control (wt) by Student's t test. (**B**) Representative blots of the polymer poly-ADP-ribose (PAR), the product of poly-ADP-ribose polymerase-1 (PARP-1) activity, in right (R) and left (L) hemispheres of control (wt, closed bars) and H^+/T^+ (open bars) mice. One control and two H^+/T^+ mice are shown. β-F1-ATPase expression is shown as loading control. Histograms show the quantification of PAR/β-F1 ratio. * and #, $P<0.05$ when compared to the right or left hemisphere of controls, respectively. (**C**) Effect of ROS scavenging (20 nM mito Q, mQ) on glutamate primed cell death in neurons derived from control (wt, closed bars) and H^+/T^+ (open bar) mice. (**D**) Blue-native immunoblot analysis of Bcl-xL immunoreactivity associated to complexes of mitochondrial OXPHOS. The migration of complex I (CI, NADH9), F0F1-ATPase (CV, β-F1-

ATPase) and Bcl-xL in control (wt) and H^+/T^+ mice is indicated. The migration of molecular mass markers is indicated to the right. (**E**) Effect of glutamate and 1 h hypoxia on cell death in primary cultures of cortical neurons derived from control (wt, closed bars) and H^+/T^+ (open bar) mice. The silencing of Bcl-xL (siBcl-xL) using β-actin as loading control is illustrated. (**A, B, C, E**) Bars are the mean ± SEM of three (**B, C, E**) or five (**A**) experiments. * and #, $P<0.05$ when compared to control (wt) or to silencing control (H^+/T^+, siCRL).

Figure 7. IF1 expression in human brain. (**A**) Western blots of the expression of IF1 in fractionated proteins from mice neurons and astrocytes using the commercial anti-mouse IF1. β-F1-ATPase (β-F1) expression is shown as loading control. Histograms show the quantification of IF1/β-F1 ratio. The data shown are mean ± SEM of 3-4 preparations. (**B,C**) Immunocytochemistry of hIF1 in human cerebral cortex. Note IF1 immunolabelling in cortical neurons of the parieto-occipital cortex and the negative labeling of astrocytes. Magnification 20x (**B**) and 63x (**C**). (**D-F**) Immunocytochemistry for IF1 in human cerebellar sections. (**D, E**): positive immunolabelling for hIF1 in Purkinje cells, granular neurons and Golgi type II neurons. Magnification 20x (**D**) and 63x (**E**). (**F**): Strong hIF1 immunolabelling in neurons of the cerebellar dentate nucleus. Magnification 20x. (**G**) The schematic illustrates the role of the over-expression of hIF1 in preconditioning of the brain. In normal mice the IF1 present is non-functional as relevant repressor of the synthetic activity of the H^+-ATP synthase either by its binding to a putative receptor (BP) and/or because of covalent modifications of the protein. The over-expression of hIF1 with higher affinity for β-F1-ATPase partially interferes with OXPHOS and promotes an enhanced glycolysis and a mild ROS signal that activates in the nucleus pathways of survival and repair enhancing the threshold level required to

execute cell death. In addition, hIF1 overexpression might affect the dimerization of the H^+-ATP synthase that is involved in PTP formation. The metabolic (red arrows) and structural (violet arrow) pathways of brain preconditioning are highlighted. Upon administration of a death stimuli hIF1 inhibits more effectively the synthase activity of the H^+-ATP synthase than endogenous IF1. By a mechanism that remains to be discovered IF1 prevents PTP opening and extensive neuronal cell death. See also Figure S10.

Figure 1

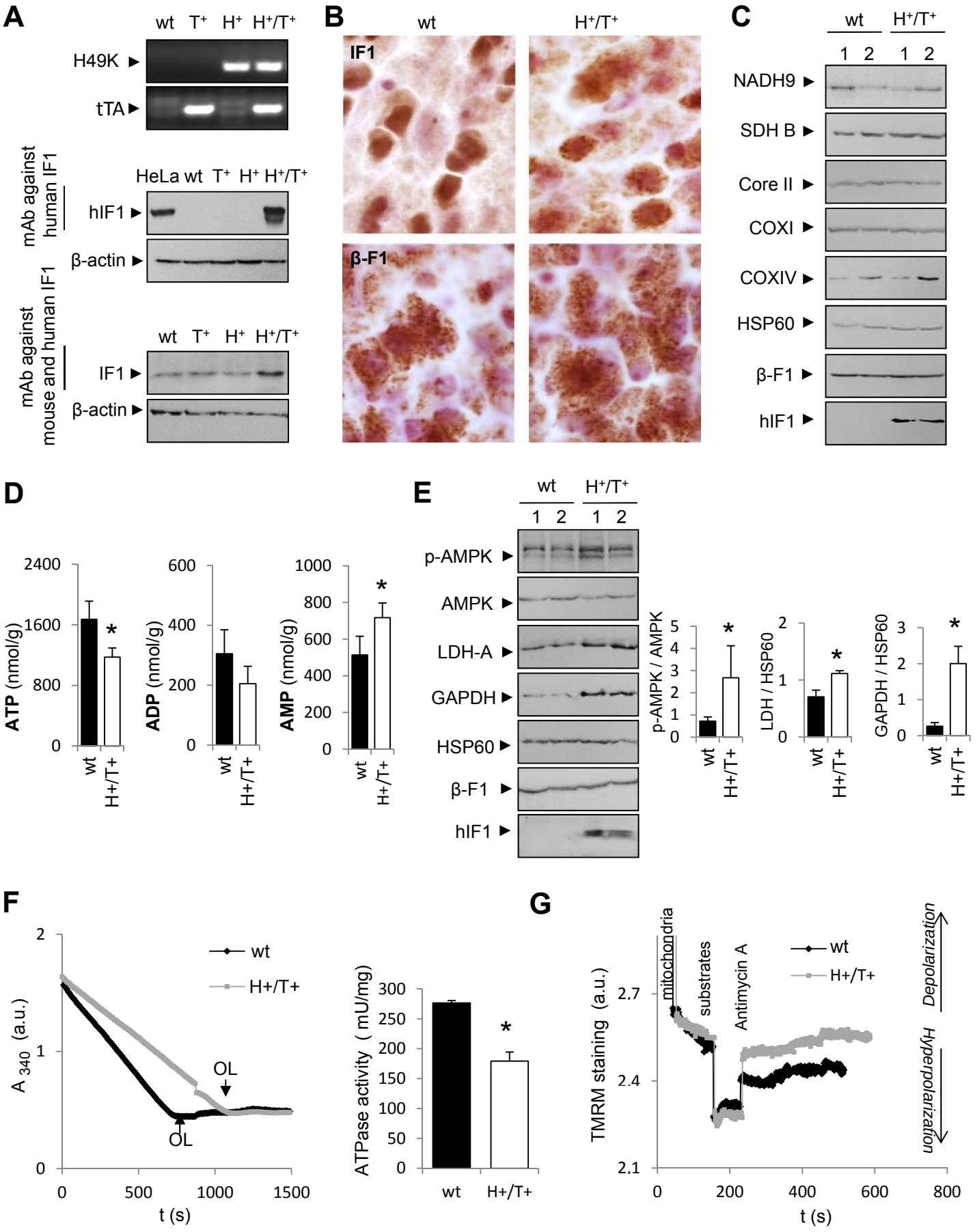
A
wt T+ H+ H+/T+
H49K
tTA
HeLa wt T+ H+ H+/T+
mAb against human IF1
hIF1
β-actin
wt T+ H+ H+/T+
mAb against mouse and human IF1
IF1
β-actin
B
wt
H+/T+
IF1
β-F1
C
wt
H+/T+
1 2 1 2
NADH9
SDH B
Core II
COXI
COXIV
HSP60
β-F1
hIF1
D
ATP (nmol/g)
ADP (nmol/g)
AMP (nmol/g)
wt
H+/T+
E
wt
H+/T+
1 2 1 2
p-AMPK
AMPK
LDH-A
GAPDH
HSP60
β-F1
hIF1
p-AMPK / AMPK
LDH / HSP60
GAPDH / HSP60
F
wt
H+/T+
A 340 (a.u.)
OL
OL
t (s)
ATPase activity (mU/mg)
G
mitochondria
substrates
Antimycin A
wt
H+/T+
TMRM staining (a.u.)
Depolarization
Hyperpolarization
t (s)

Figure 2

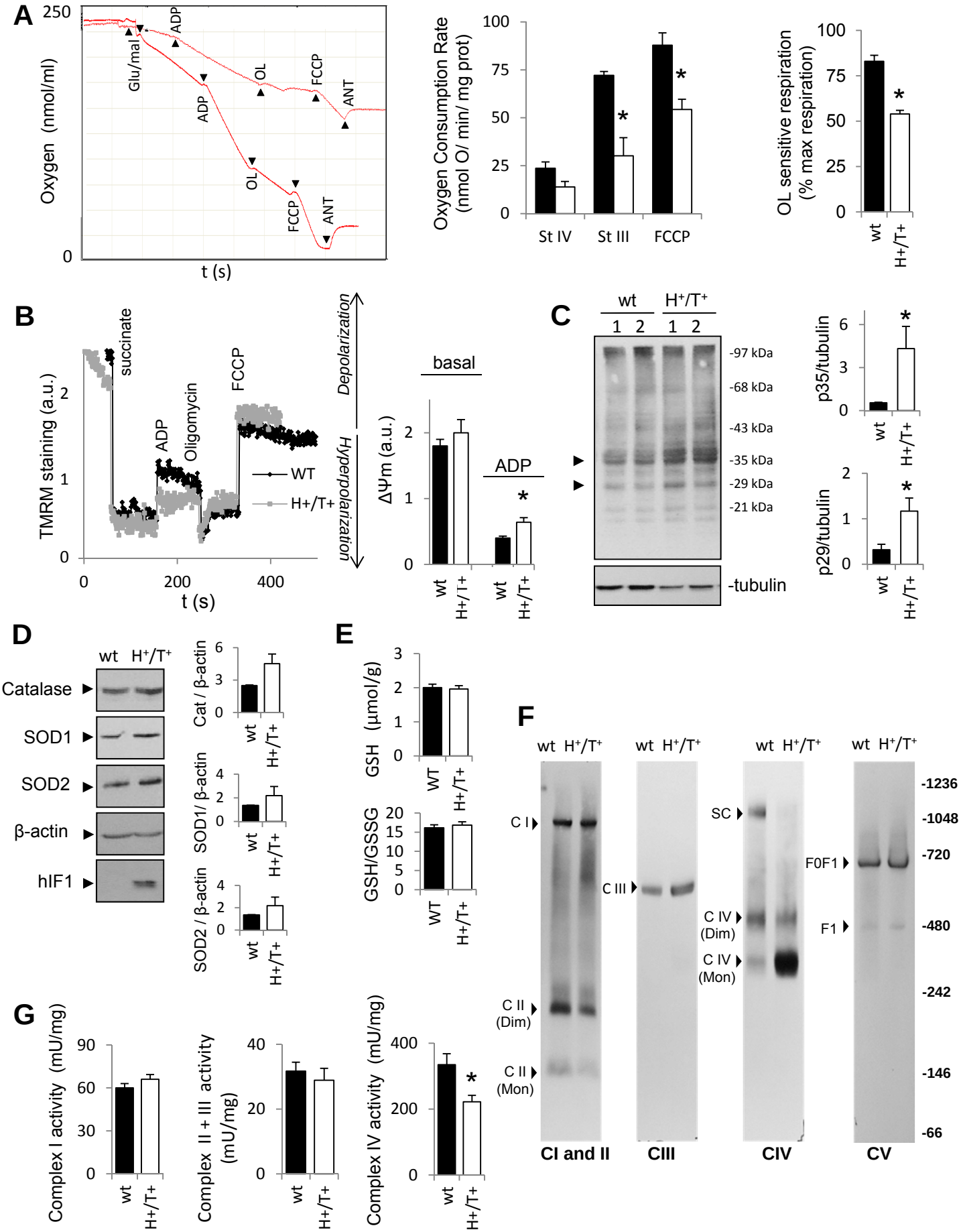
A
Oxygen (nmol/ml)
250
0
t (s)
Glu/mal
ADP
ADP
OL
FCCP
ANT
OL
FCCP
ANT
Oxygen Consumption Rate (nmol O/ min/ mg prot)
100
75
50
25
0
St IV
St III
FCCP
OL sensitive respiration (% max respiration)
wt
H+/T+
B
TMRM staining (a.u.)
succinate
ADP
Oligomycin
FCCP
WT
H+/T+
Depolarization
Hyperpolarization
t (s)
basal
ADP
ΔΨm (a.u.)
C
wt
H+/T+
1 2 1 2
-97 kDa
-68 kDa
-43 kDa
-35 kDa
-29 kDa
-21 kDa
-tubulin
p35/tubulin
p29/tubulin
D
wt H+/T+
Catalase
SOD1
SOD2
β-actin
hIF1
Cat / β-actin
SOD1/ β-actin
SOD2 / β-actin
E
GSH (µmol/g)
GSH/GSSG
WT
H+/T+
F
wt H+/T+
C I
C II (Dim)
C II (Mon)
C III
SC
C IV (Dim)
C IV (Mon)
F0F1
F1
-1236
-1048
-720
-480
-242
-146
-66
CI and II
CIII
CIV
CV
G
Complex I activity (mU/mg)
Complex II + III activity (mU/mg)
Complex IV activity (mU/mg)

Figure 3

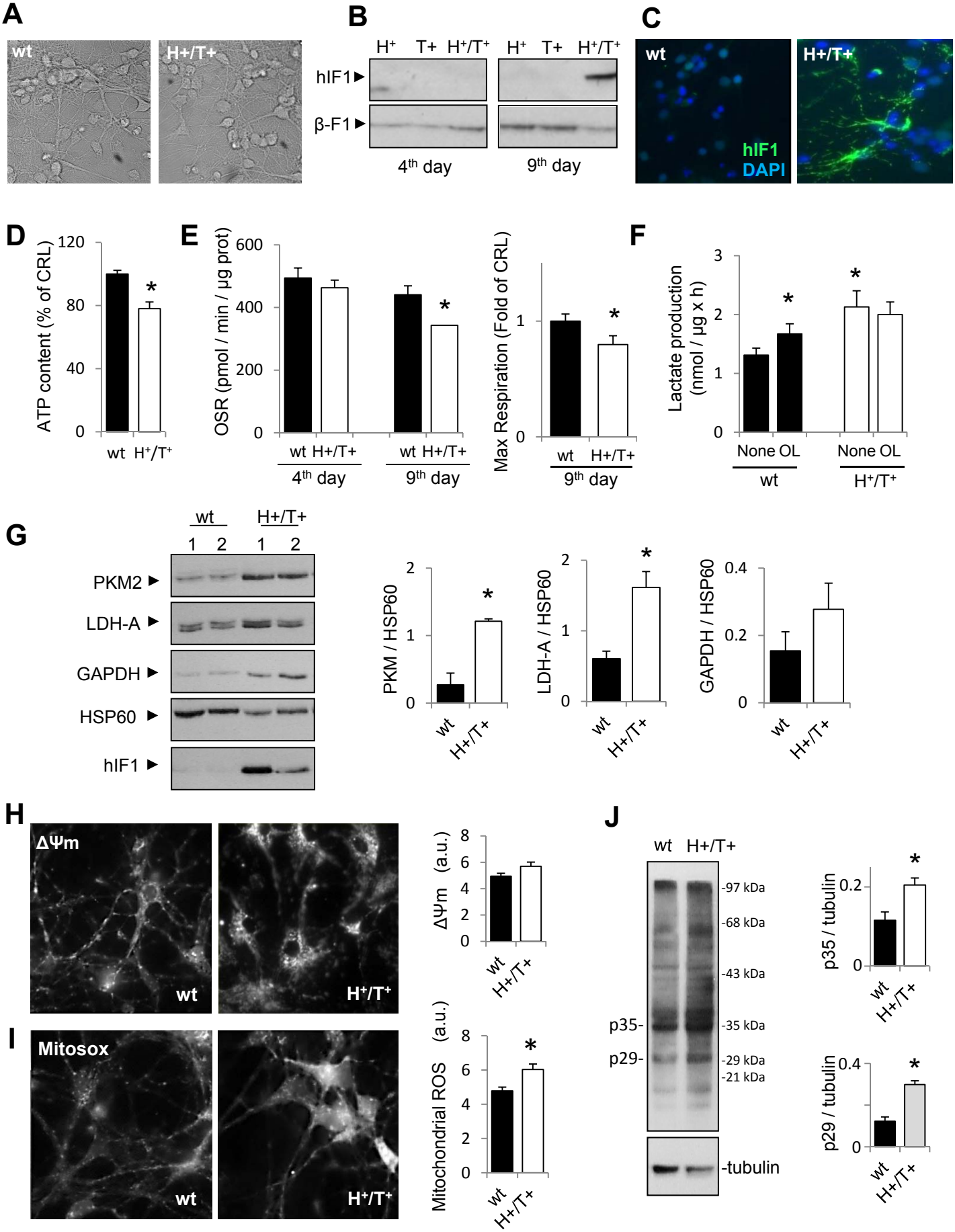
A
wt
H+/T+
B
H+ T+ H+/T+ H+ T+ H+/T+
hIF1
β-F1
4th day
9th day
C
wt
H+/T+
hIF1
DAPI
D
ATP content (% of CRL)
wt H+/T+
E
OSR (pmol / min / µg prot)
wt H+/T+ wt H+/T+
4th day 9th day
Max Respiration (Fold of CRL)
wt H+/T+
9th day
F
Lactate production (nmol / µg x h)
None OL None OL
wt H+/T+
G
wt H+/T+
1 2 1 2
PKM2
LDH-A
GAPDH
HSP60
hIF1
PKM / HSP60
LDH-A / HSP60
GAPDH / HSP60
H
ΔΨm
wt
H+/T+
ΔΨm (a.u.)
I
Mitosox
wt
H+/T+
Mitochondrial ROS (a.u.)
J
wt H+/T+
-97 kDa
-68 kDa
-43 kDa
-35 kDa
-29 kDa
-21 kDa
p35-
p29-
-tubulin
p35 / tubulin
p29 / tubulin

Figure 4

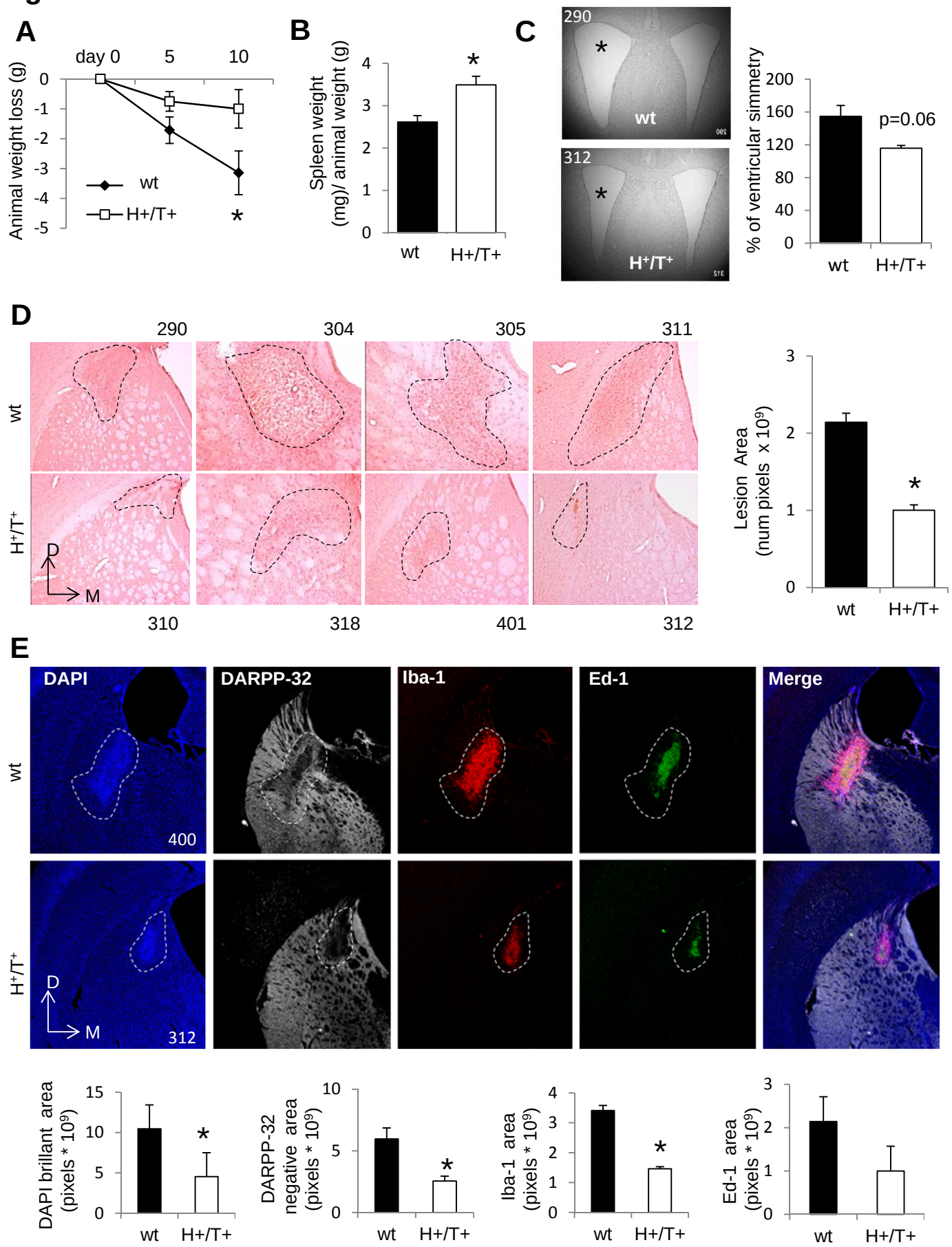
A
day 0
5
10
Animal weight loss (g)
0
-1
-2
-3
-4
-5
wt
H+/T+
*
B
Spleen weight (mg)/ animal weight (g)
4
3
2
1
0
*
wt
H+/T+
C
290
*
wt
312
*
H+/T+
% of ventricular simmetry
200
160
120
80
40
0
p=0.06
wt
H+/T+
D
290
304
305
311
wt
H+/T+
P
M
310
318
401
312
Lesion Area (num pixels x 10⁹)
3
2
1
0
*
wt
H+/T+
E
DAPI
DARPP-32
Iba-1
Ed-1
Merge
wt
H+/T+
400
312
P
M
DAPI brillant area (pixels * 10⁹)
15
10
5
0
*
wt
H+/T+
DARPP-32 negative area (pixels * 10⁹)
10
5
0
*
wt
H+/T+
Iba-1 area (pixels * 10⁹)
4
3
2
1
0
*
wt
H+/T+
Ed-1 area (pixels * 10⁹)
3
2
1
0
wt
H+/T+

Figure 5

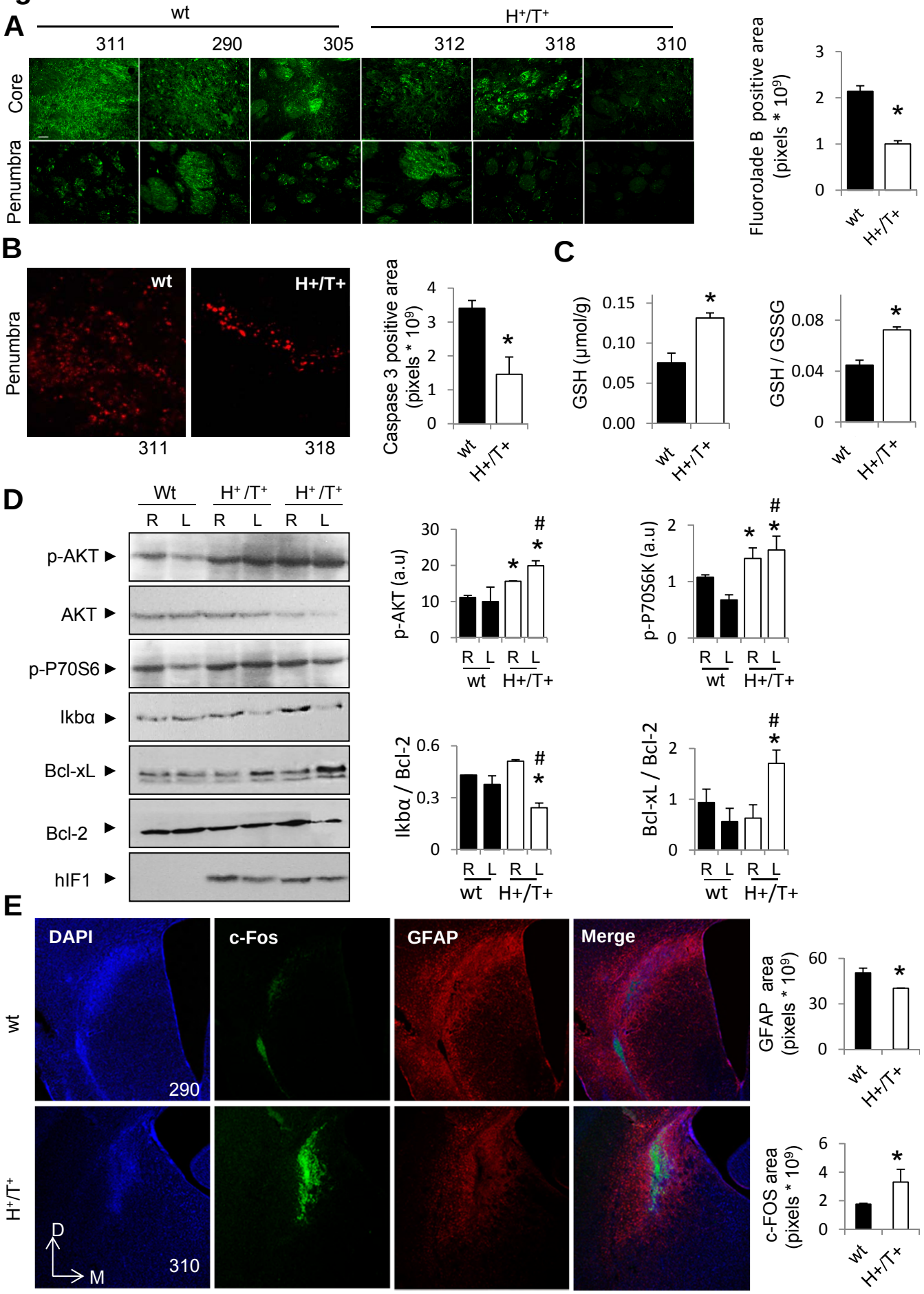
A
wt
H+/T+
311
290
305
312
318
310
Core
Penumbra
FluoroJade B positive area (pixels * 10⁹)
wt
H+/T+
B
Penumbra
wt
H+/T+
311
318
Caspase 3 positive area (pixels * 10⁹)
C
GSH (µmol/g)
GSH / GSSG
D
Wt
H+ /T+
H+ /T+
R L R L R L
p-AKT
AKT
p-P70S6
Ikbα
Bcl-xL
Bcl-2
hIF1
p-AKT (a.u)
p-P70S6K (a.u)
Ikbα / Bcl-2
Bcl-xL / Bcl-2
E
DAPI
c-Fos
GFAP
Merge
290
310
D
M
GFAP area (pixels * 10⁹)
c-FOS area (pixels * 10⁹)

Figure 6

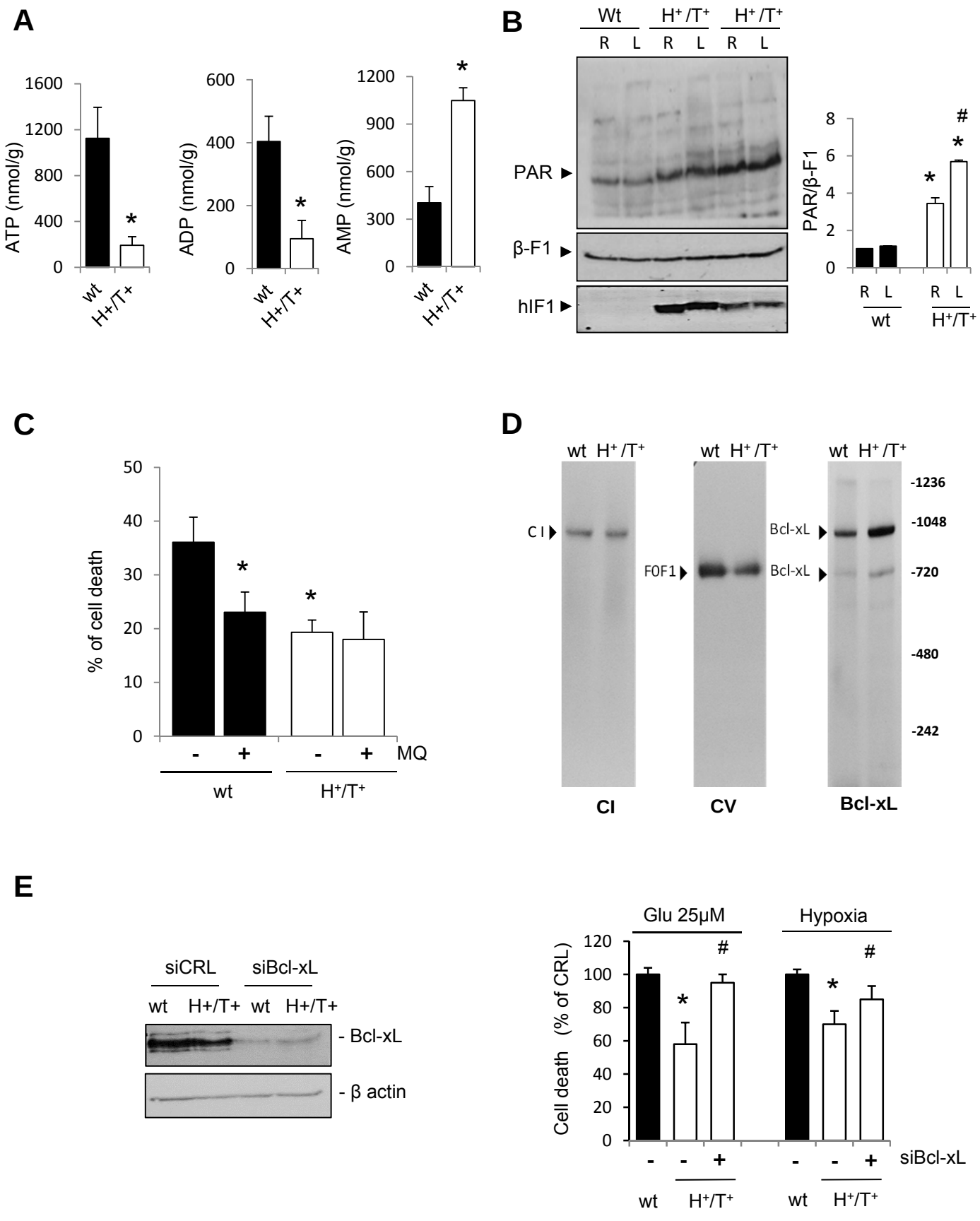
A
ATP (nmol/g)
ADP (nmol/g)
AMP (nmol/g)
wt
H+/T+
B
Wt
H+ /T+
H+ /T+
R L R L R L
PAR
β-F1
hIF1
PAR/β-F1
wt
H+/T+
C
% of cell death
MQ
wt
H+/T+
D
wt H+ /T+
CI
FOF1
Bcl-xL
-1236
-1048
-720
-480
-242
CI
CV
Bcl-xL
E
siCRL
siBcl-xL
- Bcl-xL
- β actin
Glu 25μM
Hypoxia
Cell death (% of CRL)
siBcl-xL

Figure 7

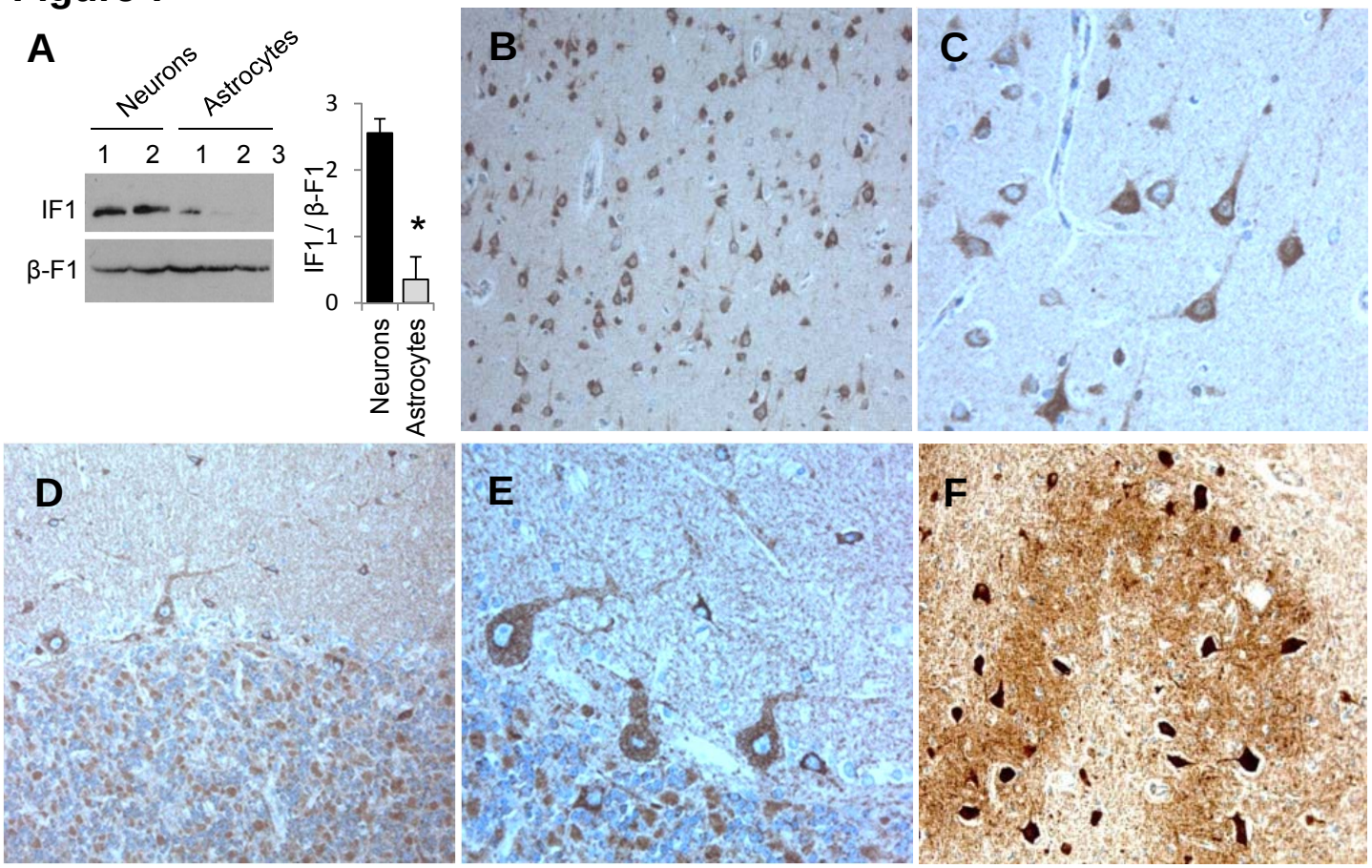
A
Neurons
Astrocytes
1 2 1 2 3
IF1
β-F1
IF1 / β-F1
3
2
1
0
*
Neurons
Astrocytes
B
C
D
E
F

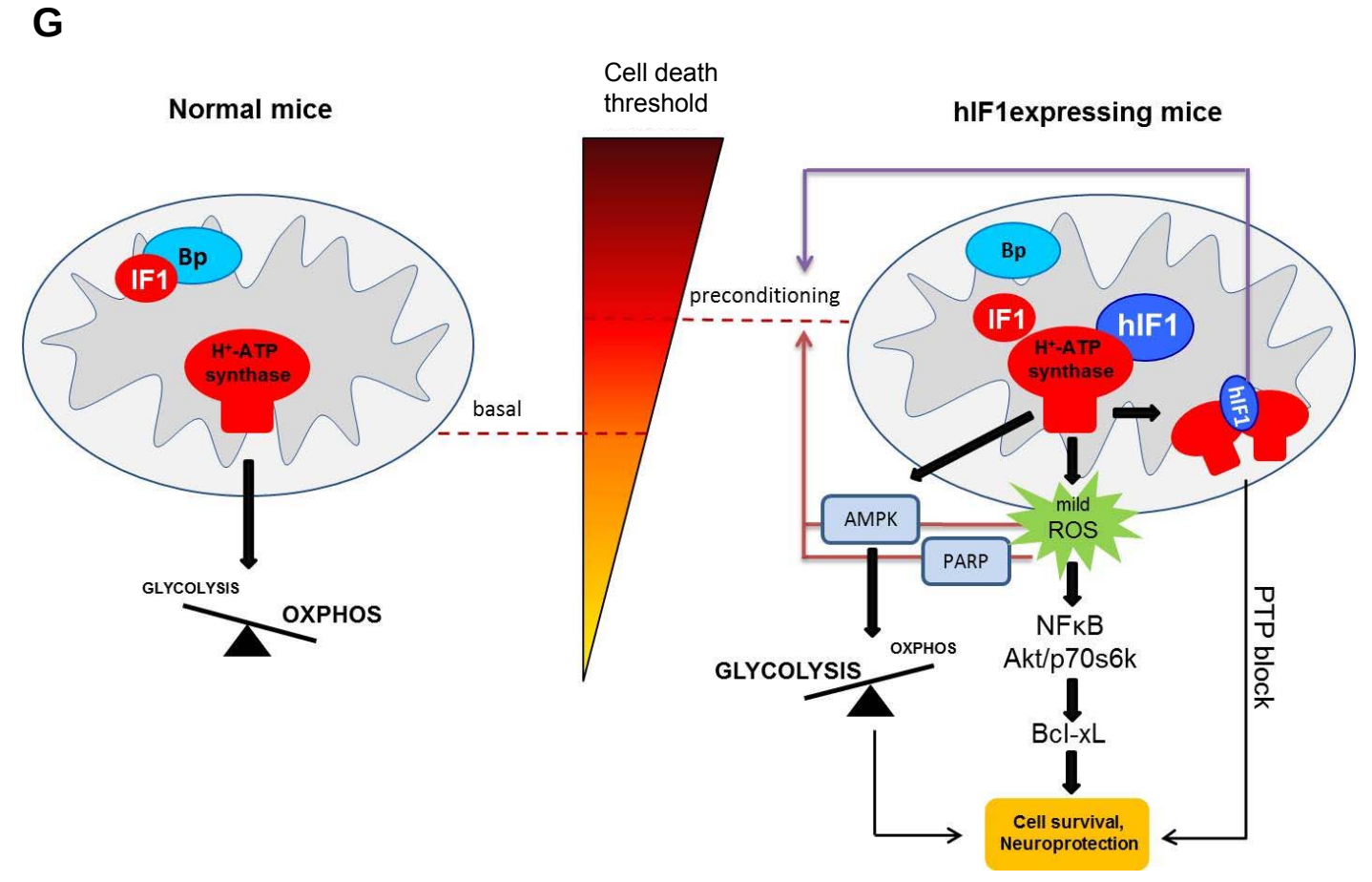
G
Normal mice
Cell death threshold
hIF1expressing mice
Bp
IF1
H⁺-ATP synthase
basal
preconditioning
GLYCOLYSIS
OXPHOS
hIF1
AMPK
PARP
mild ROS
NFκB
Akt/p70s6k
Bcl-xL
PTP block
Cell survival, Neuroprotection

Supplementary Information.

Supplementary Figures.

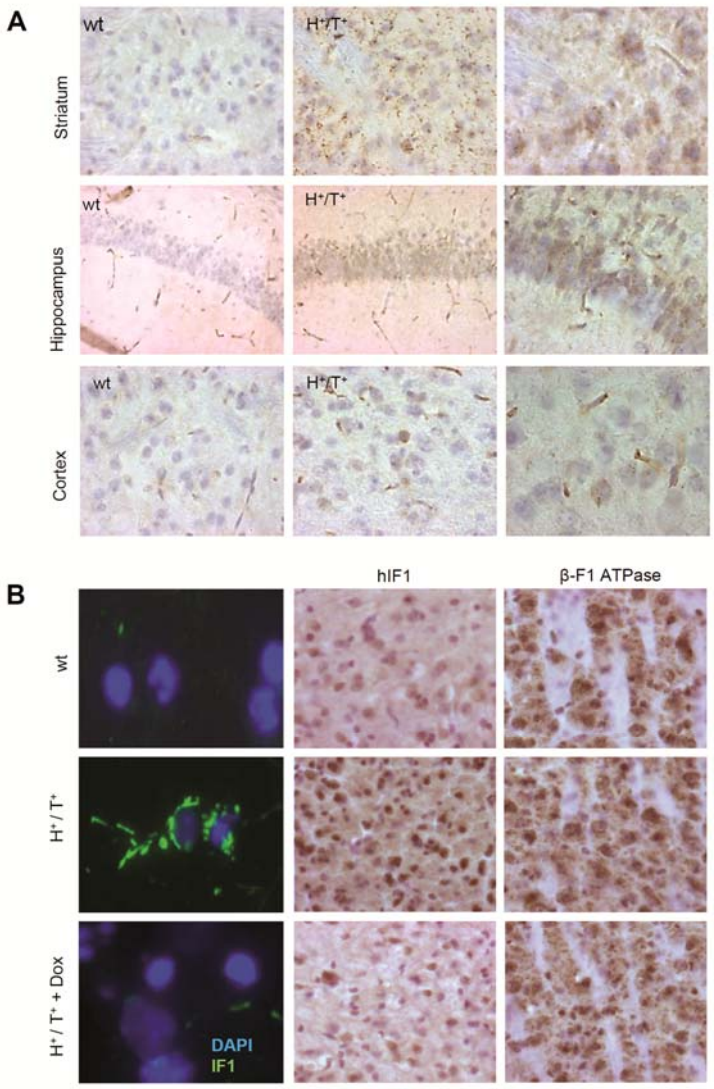

Figure S1. (**A**) Immunohistochemistry of hIF1 in brain striatum, hippocampus and cortex of control (wt) and hIF1 expressing (H^+/T^+) mice. Magnification 40x (first and second columns) and 63x (third column). (**B**) Immunofluorescence (first column) and immunohistochemistry of hIF1 and β-F1-ATPase in the brain of control (wt) and hIF1 expressing (H^+/T^+) mice. Note that the oral administration of doxycycline abrogates the expression of hIF1 in H^+/T^+ mice. Magnification 63x (first column) and 40x (second and third columns).

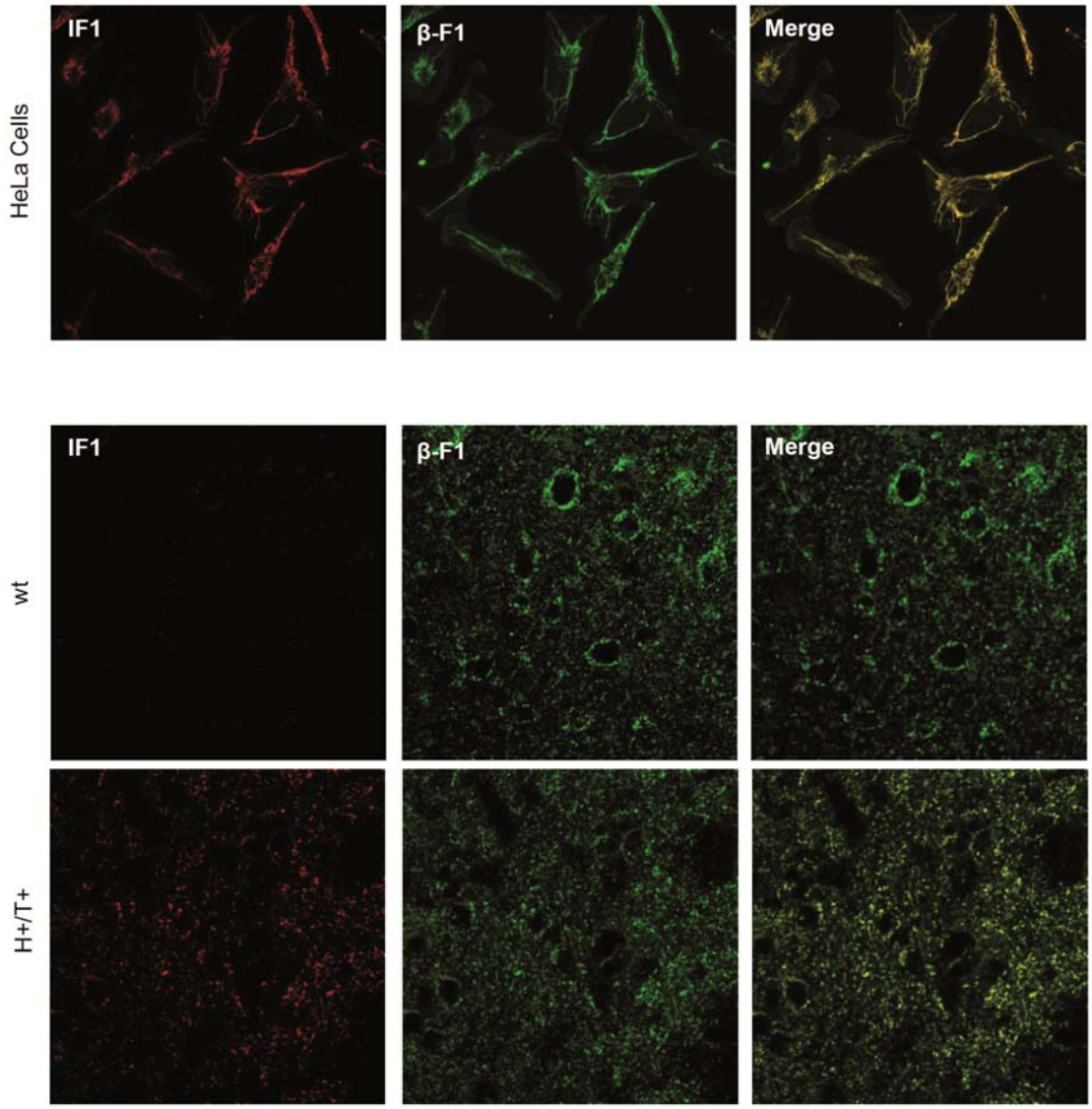

Figure S2. hIF1 is localized in mitochondria. Upper panels, HeLa cells were transfected with the pCMV-SPOR6-H49K plasmid and processed for immunofluorescene microscopy for hIF1 (red) and β-F1-ATPase (β-F1, green). Immunohistochemistry for hIF1 (red) and β-F1-ATPase (β-F1, green) in brain cortex of control (wt, middle panel) and H^+/T^+ (lower panel) mice. Magnification 40x (upper panel) and 20x (middle and lower panel). Note that hIF1 is only expressed in neurons of H^+/T^+ mice whereas β-F1-ATPase is present in glia and neurons of both phenotypes.

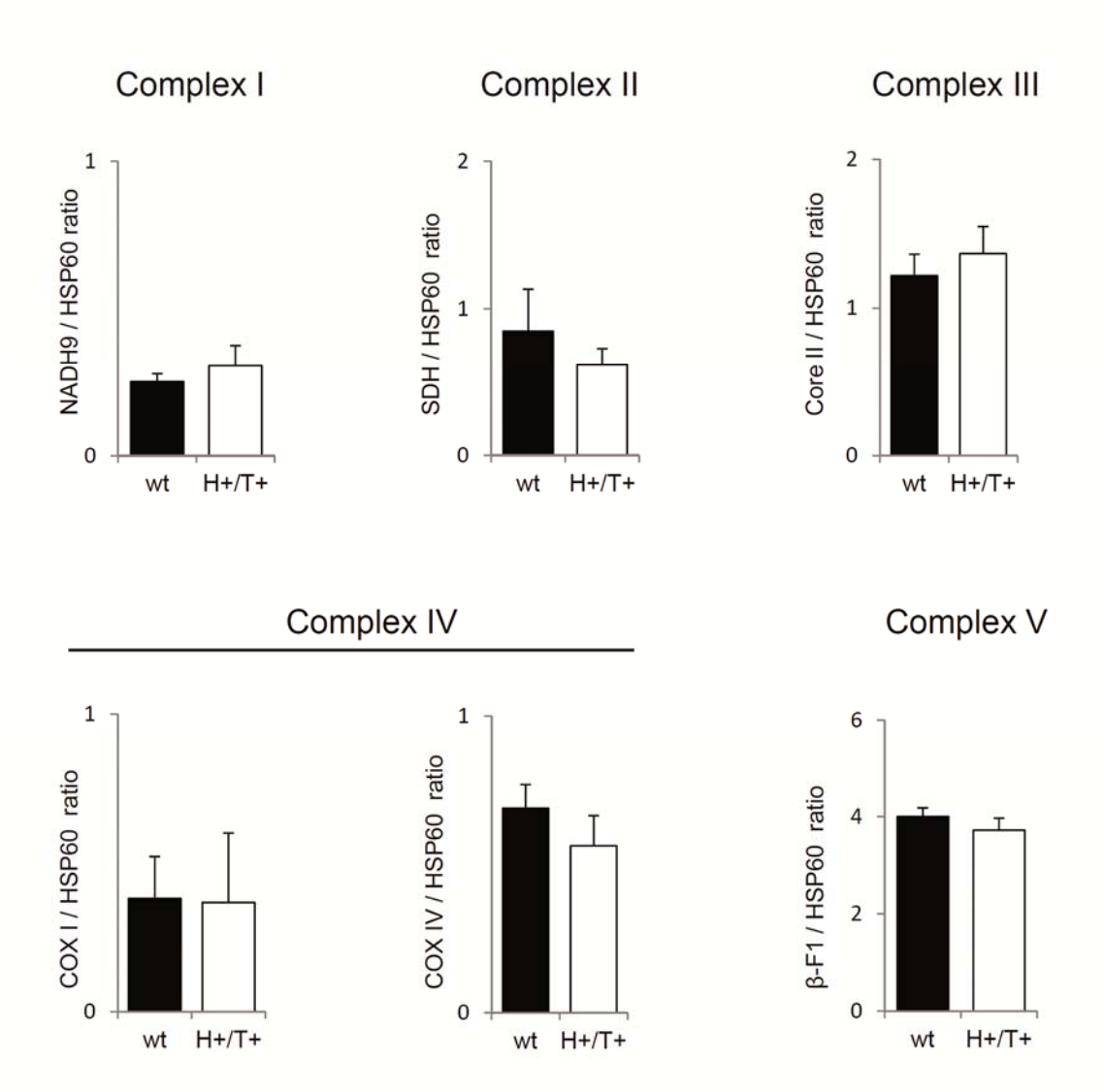

Figure S3. Quantification of the expression of OXPHOS proteins. Fractionated proteins were blotted against heat-shock protein 60 (HSP60), and mitochondrial complexes I (NADH9), II (SDH), III (Core II), IV (COXI and COX IV) and V (β-F1) in total brain extracts of wt and H+/T+ mice as shown in Fig. 1C. The data shown are mean ± SEM of 3 experiments assayed in duplicate.

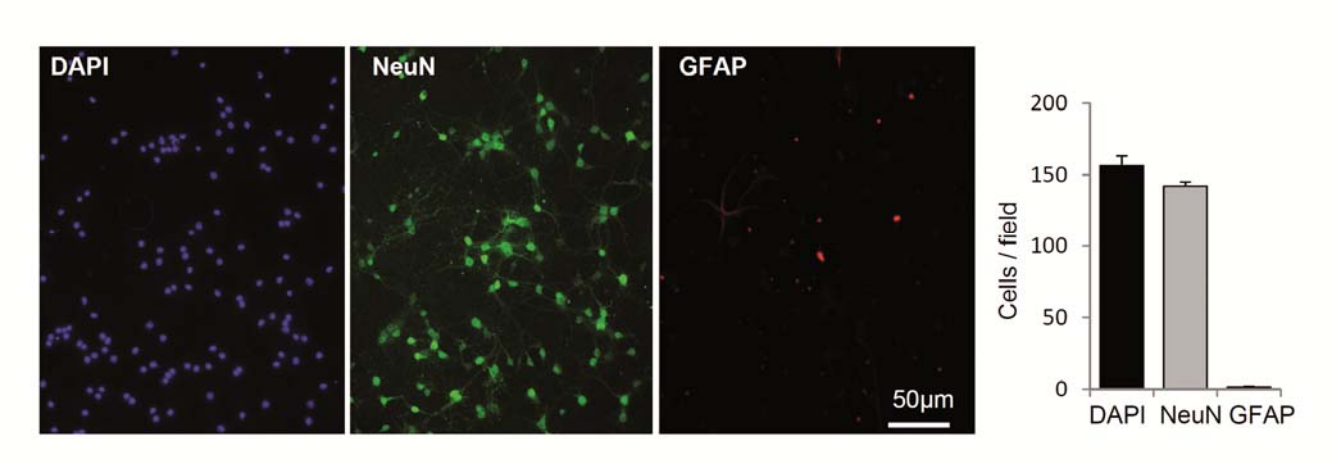

Figure S4. Nine days after seeding, the cultures revealed that they were mainly composed of neurons. Immunocytochemistry for the neuronal marker NeuN (green) and the astrocyte marker GFAP (red) in primary cultures of cortical neurons. The nuclei were stained with DAPI (blue). Histograms show the quantification of the number of each cell type per field. Magnification 10x. The data shown are mean ± SEM of 7 fields.

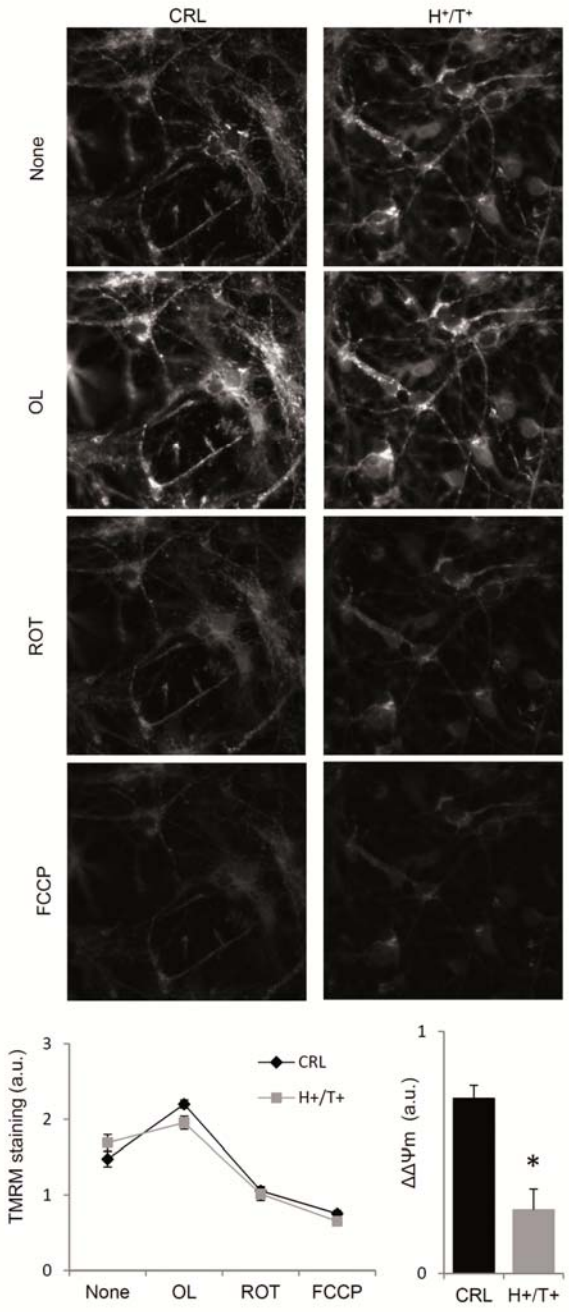

Figure S5. *In vivo* staining of $TMRM^+$ charged mitochondria from 9-10d primary cultures of cortical neurons derived from control (CRL) and H^+/T^+ embryos. Images and graph represent the sequential cytofluorometric measurements of mitochondrial membrane potential (TMRM staining, ΔΨm) in basal condition (None), after addition of 6µM oligomycin (OL), 1µM rotenone (ROT) and finally 5µM FCCP in the same field. Histograms show the quantification of ΔΨm differences between OL treated cells and basal condition. Magnification 40x. The data shown are mean ± SEM of 15 fields per condition. *, $p<0.05$ when compared to control by Student's t test.

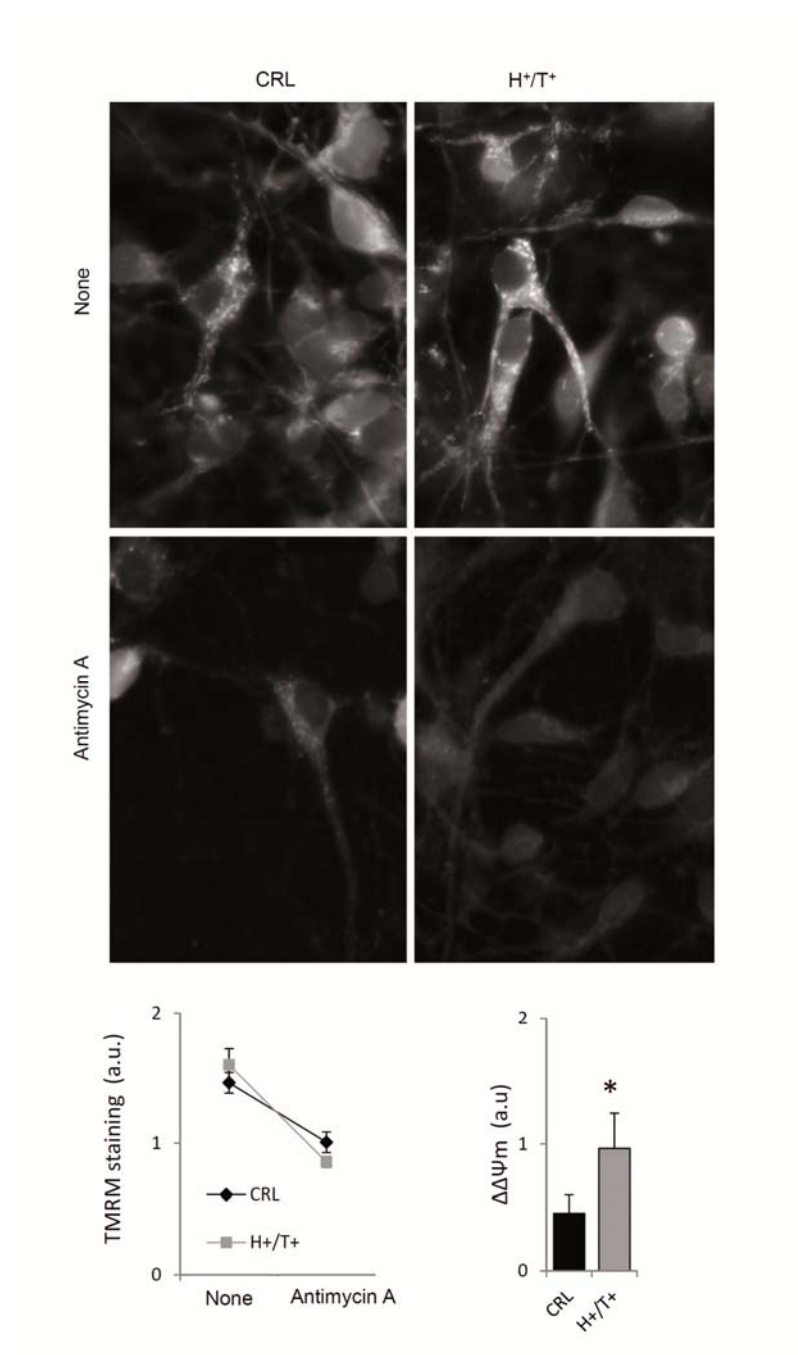

Figure S6. *In vivo* staining of $TMRM^+$ charged mitochondria from 9-10d primary cultures of cortical neurons derived from control (CRL) and H^+/T^+ embryos. Images and graph represent the sequential cytofluorometric measurements of mitochondrial membrane potential (TMRM staining, ΔΨm) in basal condition (None) and after the addition of 1µM antimycin A. Histograms show the quantification of ΔΨm differences between basal condition and antimycin treated cells. Magnification 40x. The data shown are mean ± SEM of 15 fields per condition. *, $p<0.05$ when compared to control by Student's t test.

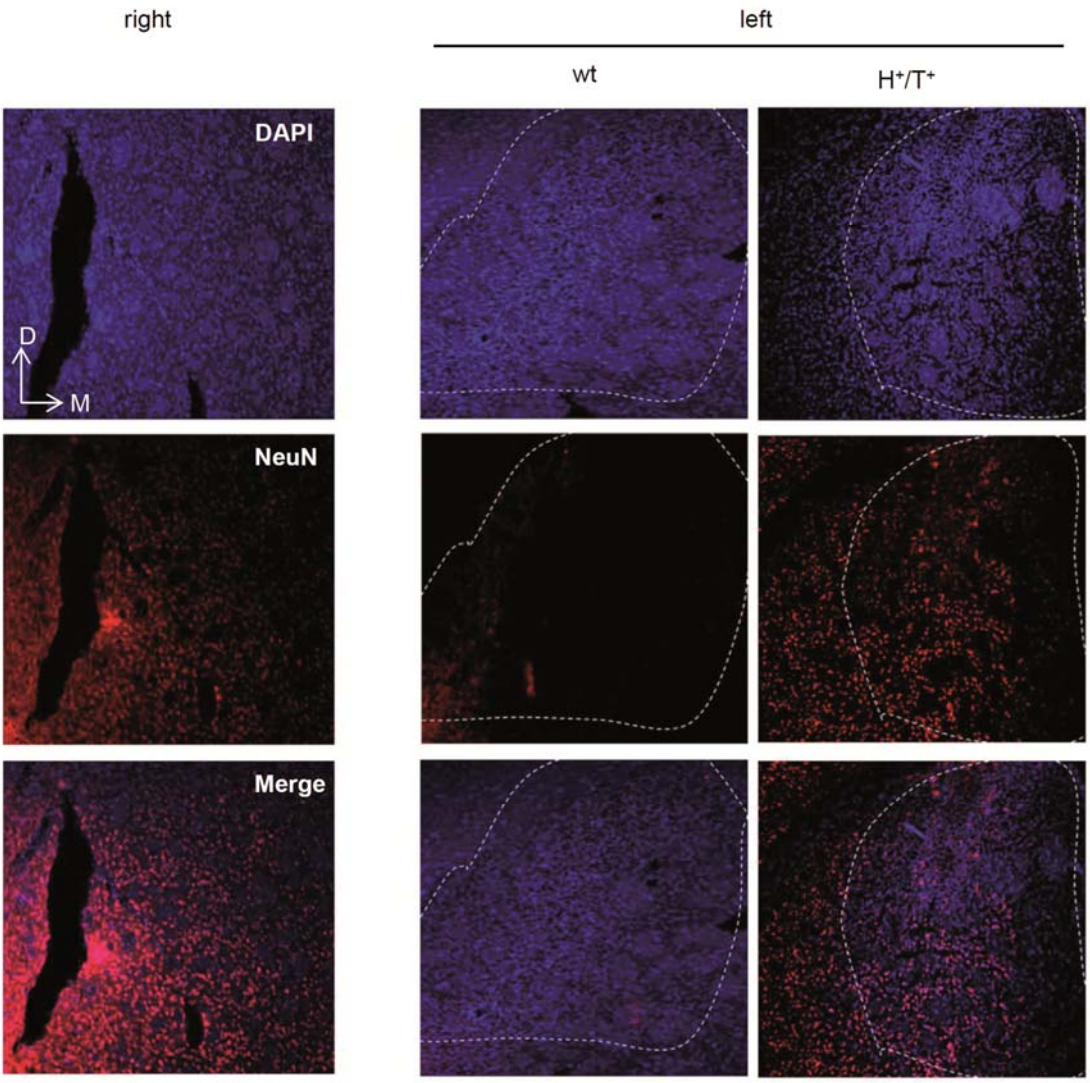

Figure S7. Immunohistochemistry for the neuronal marker NeuN (red) in right (non-damaged) and left (damaged) brain hemispheres of control (wt) and hIF1 expressing (H^+/T^+) mice. The nuclei have been stained with DAPI (blue). Magnification 10x. Note that at 20 days after surgery the striatum has already started to degenerate and the left hemisphere of control mice showed no NeuN expression in the focus of the lesion. In contrast, visible NeuN-staining was observed in H^+/T^+ mice indicating the partial protection from cell death exerted by hIF1. D, dorsal; M, medial.

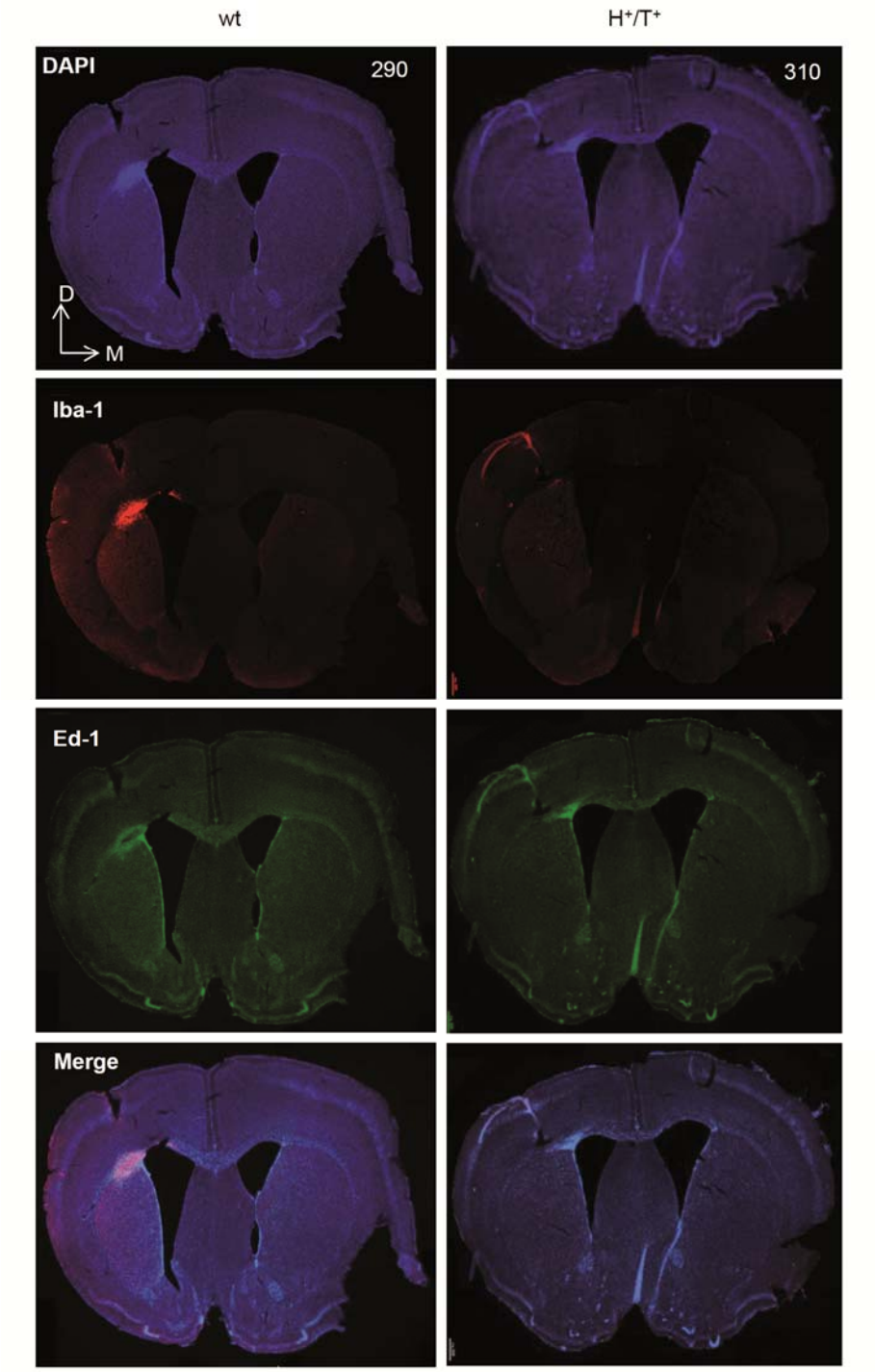

Figure S8. Representative staining of DAPI (nucleus, blue), Iba-1 (microglia, red) and Ed-1 (macrophage, green) antibodies in coronal slices of the brain in control (wt) and H^+/T^+ mice three weeks after surgery. Magnification 2.5x. Note the minor recruitment of inflamatory cells in the brain of hIF1 expressing mice.

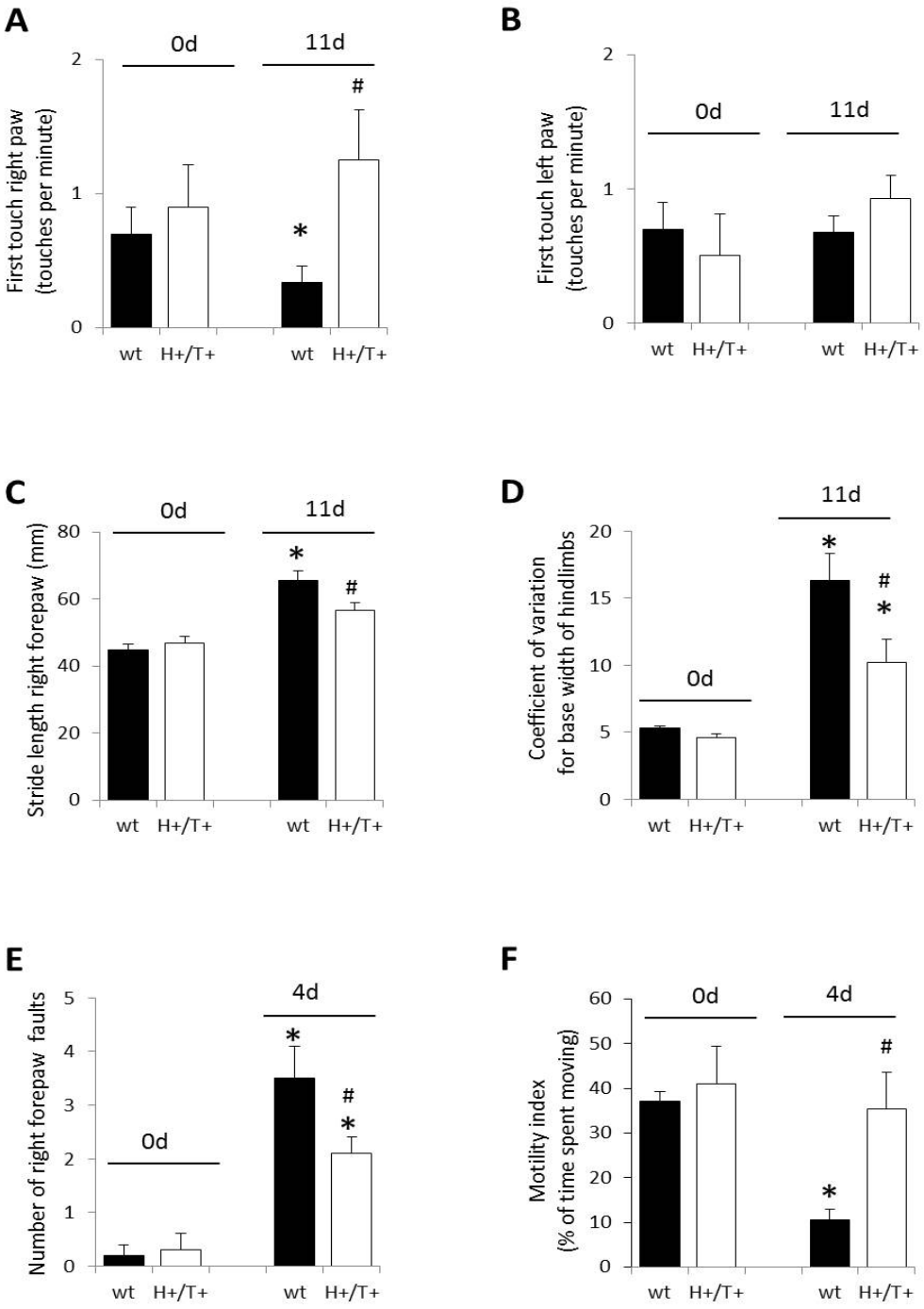

Figure S9. Locomotor evaluation indicates better performance in hIF1 expressing mice. Neurological evaluation in control (wt, closed bars) and hIF1 expressing (H^+/T^+, open bars) mice is shown. Cylinder test (**A** and **B**), foot print analysis (**C** and **D**) and grid test (**E** and **F**) before (0 d) and after four or eleven days (4 d, 11 d) post-surgery. Bars are the mean ± SEM. of ten animals. (**A**) Represents the number of the "first touch" per minute using the right paw, which is contralateral to the brain lesion while (**B**) shows

the touches of the "first touch" per minute using the ipsilateral paw. (**C**) Stride length right forepaw is reduced after lesion in H^+/T^+ mice when compared to control (wt) animals. (**D**) Gait variability for base width of hindlimbs studied using the coefficient of variation. (**E**) Number of contralateral paw slips through the grid is shown at 4 days post-surgery. (**F**) Motility index was strongly diminished in control (wt) animals. (**A-F**) *, $P<0.05$ when compared to control at day 0. #, $P<0.05$ when compared to control at day 4 or 11 post-surgery.

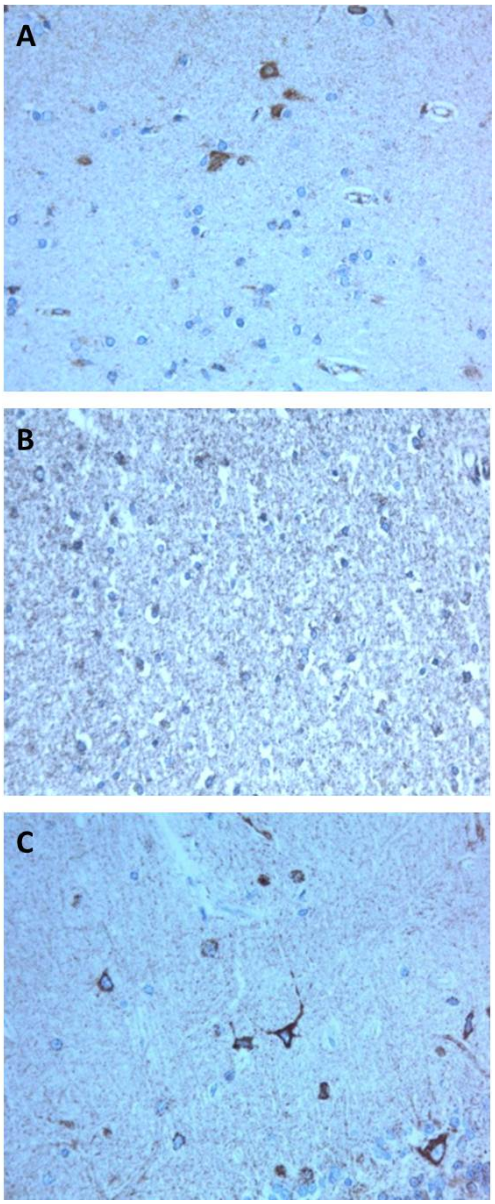

Figure S10. Immunocytochemistry of hIF1 in human cerebral cortex (**A, B**) and cerebellum (**C**) sections. (**A**) Cortico-subcortical area showing positive neurons and negative astrocytes. (**B**) White matter. Negative immunolabelling for astrocytes and oligodendrocytes. (**C**) Positive immunostaining in basket cells of the molecular layer. Magnification 63x. Other hIF1 positive neuronal types are: neurons from the diencephalic, thalamic, hypothalamic and mesencephalic nuclei, lateral and medial corpus geniculatum, motor and sensitive brain-stem nuclei, inferior olives, Clarke columns and motor and sensitive neurons from the spinal cord (data no shown).

Supplementary Videos 1, 2, 3 and 4. Grid test in control mice 9, 290, 304 and 305 at 11 days post-surgery.

Supplementary Videos 5, 6, 7 and 8. Grid test in hIF1 expressing mice 296, 312, 345 and 346 at 11 days post-surgery.

Supplementary Materials and Methods.

Western Blot and Protein carbonylation antibodies. The primary monoclonal antibodies developed in our lab and used in this study were: anti-HSP60 (1:5,000), anti-NADH-9 (1:1,000), anti-β-F1-ATPase (1:20,000), anti-LDH-A (1:1,000), anti-GAPDH (1:20,000) and anti-PKM2 (1:1,000) (Acebo et al., 2009). The monoclonal antibody specifically recognizing the human (Sanchez-Cenizo et al., 2010) and mouse (Molecular Probes) IF1 proteins were used at 1:200 dilution. Other antibodies used were: anti-β-actin (1:20,000), anti-tubulin (1:5,000) and anti-catalase (1:5,000) from Sigma-Aldrich; anti-SDH (1:1000) from Life Technologies; anti-Complex III subunit Core 2 (1:1,000), anti-COXI (1:1,000), anti-COXIV (1:1,000) and anti-SOD1 (1:1,000) from Abcam; anti-SOD2 (1:5,000) from Santa Cruz Biotechnology, Inc.; anti-PAR (1:1000) from Enzo Life Science Inc.; anti-IκBα (1:1,000), anti-Akt (1:1,000), anti-p-Akt (1:1,000), anti-p-p70S6K (1:1,000), anti-Bcl-xL (1:1,000) and anti-Bcl-2 (1:1,000) from Cell Signaling Technology Inc. Peroxidase-conjugated anti-mouse, anti-goat or anti-rabbit IgGs (Nordic Immunology; 1:3,000) were used as secondary antibodies.

For the determination of protein carbonylation, dinitrophenylhydrazine (DNPH) derivatization was carried out on 20 μg of proteins derived from brain or neuronal extracts. Samples were fractionated on SDS–12% PAGE. The antibodies used were rabbit anti-DNP (1:150) and goat anti-rabbit IgGs (1:300). The blots were revealed using the ECL® reagent (Amersham Pharmacia Biotech). The intensity of the bands was quantified using a Kodak DC120 digital camera and the Kodak 1D Analysis Software.

Supplementary References.

Acebo, P., Giner, D., Calvo, P., Blanco-Rivero, A., Ortega, A.D., Fernandez, P.L., Roncador, G., Fernandez-Malave, E., Chamorro, M., and Cuezva, J.M. (2009) Cancer abolishes the tissue type-specific differences in the phenotype of energetic metabolism. *Transl Oncol* **2**: 138-145.

Sanchez-Cenizo L, Formentini L, Aldea M, Ortega AD, Garcia-Huerta P, Sanchez-Arago M, Cuezva JM (2010) Up-regulation of the ATPase inhibitory factor 1 (IF1) of the mitochondrial H+-ATP synthase in human tumors mediates the metabolic shift of cancer cells to a Warburg phenotype. J Biol Chem 285: 25308-25313